OPEN ACCESS



EP241021a: A Months-duration X-Ray Transient with Luminous Optical and Radio Emission

```
Xinwen Shu<sup>1</sup>, Lei Yang<sup>1</sup>, Haonan Yang<sup>2</sup>, Fan Xu<sup>1</sup>, Jin-Hong Chen<sup>3</sup>, Rob A. J. Eyles-Ferris<sup>4</sup>, Lixin Dai<sup>3</sup>, Yunwei Yu<sup>5</sup>, Rong-Feng Shen<sup>6</sup>, Luming Sun<sup>1</sup>, Hucheng Ding<sup>1</sup>, WeiKang Zheng<sup>7</sup>, Ning Jiang<sup>8</sup>, Wenxiong Li<sup>2</sup>, Ning-Chen Sun<sup>2,9,10</sup>, Dong Xu<sup>2,11</sup>, Zhumao Zhang<sup>1</sup>, Chichuan Jin<sup>2,9,10</sup>, Arne Rau<sup>12</sup>, Tinggui Wang<sup>13</sup>, Xue-feng Wu<sup>14</sup>, Weimin Yuan<sup>2</sup>, Bing Zhang<sup>3,15</sup>, Kirpal Nandra<sup>12</sup>, Alexei V. Filippenko<sup>7</sup>, Frédérick Poidevin<sup>16,17</sup>, Roberto Soria<sup>2,18,19</sup>, Amit Kumar<sup>20</sup>, David S. Aguado<sup>16,17</sup>, Fangxia An<sup>21</sup>, Tao An<sup>2,2,3</sup>, Jie An<sup>2,9</sup>, Moira Andrews<sup>24</sup>,
Rungrit Anutarawiramkul<sup>25</sup>, Pietro Baldini<sup>12</sup>, Thomas G. Brink<sup>7</sup>, Pathompong Butpan<sup>25</sup>, Zhiming Cai<sup>26</sup>, Alberto J. Castro-Tirado<sup>27,28</sup>, Huaqing Cheng<sup>2</sup>, Weiwei Cui<sup>29</sup>, Joseph Farah<sup>24,30</sup>, Shaoyu Fu<sup>31</sup>, Johan P.U. Fynbo<sup>32,33</sup>, Xing Gao<sup>34</sup>, Dawei Han<sup>29</sup>, Xuhui Han<sup>2</sup>, D. Andrew Howell<sup>24,30</sup>, Jingwei Hu<sup>2</sup>, Shuaiqing Jiang<sup>2,9</sup>, Brajesh Kumar<sup>35,36</sup>, Weihua Lei<sup>31</sup>, Dongyue Li<sup>2</sup>, Chengkui Li<sup>29</sup>, Huaqiu Liu<sup>26</sup>, Xing Liu<sup>2,9</sup>, Yuan Liu<sup>2</sup>, Xiaowei Liu<sup>35,36</sup>, Alicia López-Oramas<sup>16,17</sup>, David López Fernández-Nespral<sup>16,17</sup>, Justyn R. Maund<sup>20</sup>, Curtis McCully<sup>24,30</sup>, Zexi Niu<sup>2,9</sup>, Magna Nayaomas<sup>24,30</sup>, Paul O'Phin<sup>4</sup>, Haiyu Pan<sup>2</sup>, Yu Pan<sup>35,36</sup>, Estafanio Padillo Congalor<sup>37</sup>
         Megan Newsome<sup>24,30</sup>, Paul O'Brien<sup>4</sup>, Haiwu Pan<sup>2</sup>, Yu Pan<sup>35,36</sup>, Estefania Padilla Gonzalez<sup>37</sup>,

Ismael Pérez-Fournon<sup>16,17</sup>, Walter Silima<sup>38</sup>, Hui Sun<sup>2</sup>, Shengli Sun<sup>39</sup>, Xiaojin Sun<sup>39</sup>, Giacomo Terreran<sup>40</sup>, Samaporn Tinyanont<sup>25</sup>, Junxian Wang<sup>13</sup>, Yanan Wang<sup>2</sup>, Yun Wang<sup>41</sup>, Klaas Wiersema<sup>42</sup>, Yunfei Xu<sup>2</sup>, Yongquan Xue<sup>13</sup>, Yi Yang<sup>7,43</sup>, Fabao Zhang<sup>1</sup>, Juan Zhang<sup>29</sup>, Pinpin Zhang<sup>2</sup>, Wenda Zhang<sup>2</sup>, Yonghe Zhang<sup>26</sup>,
Haisheng Zhao<sup>29</sup>, Zipei Zhu<sup>2</sup>, Liping Xin<sup>2</sup>, Zhuheng Yao<sup>2</sup>, Bertrand Cordier<sup>44</sup>, Jianyan Wei<sup>2</sup>, Yulei Qiu<sup>2</sup>, and Frédéric Daigne<sup>45</sup>
Department of Physics, Anhui Normal University, Wuhu, Anhui, 241002, People's Republic of China; xwshu@ahnu.edu.cn
                                              National Astronomical Observatories, Chinese Academy of Sciences, Beijing 100101, People's Republic of China Department of Physics, The University of Hong Kong, Pokfulam Road, Hong Kong, People's Republic of China
                                                            School of Physics and Astronomy, University of Leicester, University Road, Leicester, LE1 7RH, UK
                                                      School of Physics and Astronomy, Chrysisty of Eccessity, Chrysisty, Coax, 2018-25, 2018-25, 2018-25, 2018-25, 2018-25, 2018-25, 2018-25, 2018-25, 2018-25, 2018-25, 2018-25, 2018-25, 2018-25, 2018-25, 2018-25, 2018-25, 2018-25, 2018-25, 2018-25, 2018-25, 2018-25, 2018-25, 2018-25, 2018-25, 2018-25, 2018-25, 2018-25, 2018-25, 2018-25, 2018-25, 2018-25, 2018-25, 2018-25, 2018-25, 2018-25, 2018-25, 2018-25, 2018-25, 2018-25, 2018-25, 2018-25, 2018-25, 2018-25, 2018-25, 2018-25, 2018-25, 2018-25, 2018-25, 2018-25, 2018-25, 2018-25, 2018-25, 2018-25, 2018-25, 2018-25, 2018-25, 2018-25, 2018-25, 2018-25, 2018-25, 2018-25, 2018-25, 2018-25, 2018-25, 2018-25, 2018-25, 2018-25, 2018-25, 2018-25, 2018-25, 2018-25, 2018-25, 2018-25, 2018-25, 2018-25, 2018-25, 2018-25, 2018-25, 2018-25, 2018-25, 2018-25, 2018-25, 2018-25, 2018-25, 2018-25, 2018-25, 2018-25, 2018-25, 2018-25, 2018-25, 2018-25, 2018-25, 2018-25, 2018-25, 2018-25, 2018-25, 2018-25, 2018-25, 2018-25, 2018-25, 2018-25, 2018-25, 2018-25, 2018-25, 2018-25, 2018-25, 2018-25, 2018-25, 2018-25, 2018-25, 2018-25, 2018-25, 2018-25, 2018-25, 2018-25, 2018-25, 2018-25, 2018-25, 2018-25, 2018-25, 2018-25, 2018-25, 2018-25, 2018-25, 2018-25, 2018-25, 2018-25, 2018-25, 2018-25, 2018-25, 2018-25, 2018-25, 2018-25, 2018-25, 2018-25, 2018-25, 2018-25, 2018-25, 2018-25, 2018-25, 2018-25, 2018-25, 2018-25, 2018-25, 2018-25, 2018-25, 2018-25, 2018-25, 2018-25, 2018-25, 2018-25, 2018-25, 2018-25, 2018-25, 2018-25, 2018-25, 2018-25, 2018-25, 2018-25, 2018-25, 2018-25, 2018-25, 2018-25, 2018-25, 2018-25, 2018-25, 2018-25, 2018-25, 2018-25, 2018-25, 2018-25, 2018-25, 2018-25, 2018-25, 2018-25, 2018-25, 2018-25, 2018-25, 2018-25, 2018-25, 2018-25, 2018-25, 2018-25, 2018-25, 2018-25, 2018-25, 2018-25, 2018-25, 2018-25, 2018-25, 2018-25, 2018-25, 2018-25, 2018-25, 2018-25, 2018-25, 2018-25, 2018-25, 2018-25, 2018-25, 2018-25, 2018-25, 2018-25, 2018-25, 2018-25, 2018-25, 2018-25, 2018-25, 2018-25, 2018-25, 2018-25, 2018-25, 2018-25, 2018-25, 2018-25, 2018-25, 2018-25, 2018-25, 2018-25, 2
                                                                            Department of Astronomy, University of California, Berkeley, CA 94720-3411, USA
                                 <sup>8</sup> Department of Astronomy, University of Science and Technology of China, Hefei, Anhui 230026, People's Republic of China
                           School of Astronomy and Space Science, University of Chinese Academy of Sciences, Beijing 100049, People's Republic of China
                                     Institute for Frontier in Astronomy and Astrophysics, Beijing Normal University, Beijing 102206, People's Republic of China
                                                                             Altay Astronomical Observatory, Altay, Xinjiang 836500, People's Republic of China
                                                           <sup>12</sup> Max-Planck-Institut für extraterrestrische Physik, Giessenbachstrasse 1, 85748 Garching, Germany
                                       <sup>13</sup> Department of Astronomy, University of Science and Technology of China, Hefei, 230026, People's Republic of China
                                                        Purple Mountain Observatory, Chinese Academy of Sciences, Nanjing 210023, People's Republic of China
                              Nevada Center for Astrophysics and Department of Physics and Astronomy, University of Nevada Las Vegas, NV 89154, USA

16 Instituto de Astrofísica de Canarias, E-38205 La Laguna, Tenerife, Spain
                                                               <sup>17</sup> Departamento de Astrofísica, Universidad de La Laguna, E-38206 La Laguna, Tenerife, Spain
                                                    18 INAF-Osservatorio Astrofisico di Torino, Strada Osservatorio 20, I-10025 Pino Torinese, Italy
19 Sydney Institute for Astronomy, School of Physics A28, The University of Sydney, NSW 2006, Australia
20 Department of Physics, Royal Holloway—University of London, Egham, TW20 0EX, UK
                                                         <sup>21</sup> Yunnan Observatories, Chinese Academy of Sciences, Kunming 650216, People's Republic of China
                        22 Shanghai Astronomical Observatory, Chinese Academy of Sciences, 80 Nandan Road, Shanghai 200030, People's Republic of China
                        23 State Key Laboratory of Radio Astronomy and Technology, A20 Datun Road, Chaoyang District, Beijing, People's Republic of China
                                                                         Las Cumbres Observatory, 6740 Cortona Drive, Suite 102, Goleta, CA 93117-5575, USA
                                          <sup>25</sup> National Astronomical Research Institute of Thailand, 260 Moo 4, Donkaew, Maerim, Chiang Mai 50180, Thailand
                                       <sup>26</sup> Innovation Academy for Microsatellites, Chinese Academy of Sciences, Shanghai 201210, People's Republic of China
                                                         Instituto de Astrofísica de Andalucía (IAA-CSIC), Glorieta de la Astronomía s/n, 18008 Granada, Spain
<sup>28</sup> Ingeniería de Sistemas y Automática, Universidad de Málaga, Unidad Asociada al CSIC por el IAA, Escuela de Ingenierías Industriales, Arquitecto Francisco
                                                                                                                Peñalosa, 6, Campanillas, 29071 Málaga, Spain
       <sup>29</sup> Key Laboratory of Particle Astrophysics, Institute of High Energy Physics, Chinese Academy of Sciences, Beijing 100049, People's Republic of China Department of Physics, University of California, Santa Barbara, CA 93106-9530, USA
                Department of Astronomy, School of Physics, Huazhong University of Science and Technology, Wuhan, 430074, People's Republic of China

Cosmic Dawn Center (DAWN), Copenhagen 2200, Denmark
                                                                                 <sup>33</sup> Niels Bohr Institute, University of Copenhagen, Copenhagen 2200, Denmark
                                   <sup>34</sup> Xinjiang Astronomical Observatory, Chinese Academy of Sciences, Urumqi, Xinjiang 830011, People's Republic of China
                    35 South-Western Institute for Astronomy Research (SWIFAR), Yunnan University, Kunming, Yunnan 650500, People's Republic of China
                               Key Laboratory of Survey Science of Yunnan Province, Yunnan University, Kunming, Yunnan 650500, People's Republic of China
                                                                          Space Telescope Science Institute, 3700 San Martin Drive, Baltimore, MD 21218, USA
  <sup>38</sup> Inter-University Institute for Data Intensive Astronomy (IDIA), Department of Astronomy, University of Cape Town, 7701 Rondebosch, Cape Town, South
                                                                                                                                                         Africa
                                       <sup>39</sup> Shanghai Institute of Technical Physics, Chinese Academy of Sciences, Shanghai 200083, People's Republic of China
                                                                              Adler Planetarium, 1300 South Dusable Lake Shore Drive, Chicago, IL 60605, USA
<sup>41</sup> Key Laboratory of Dark Matter and Space Astronomy, Purple Mountain Observatory, Chinese Academy of Sciences, Nanjing 210023, People's Republic of China
                                                                          Centre for Astrophysics Research, University of Hertfordshire, Hatfield AL10 9AB, UK
                                                                      <sup>43</sup> Physics Department, Tsinghua University, Beijing, 100084, People's Republic of China <sup>44</sup> CEA Paris-Saclay, Irfu/D'epartement d'Astrophysique, 9111 Gif sur Yvette, France
```

⁴⁵ Sorbonne Universit'e, CNRS, UMR 7095, Institut d'Astrophysique de Paris, 98 bis bd Arago, F-75014 Paris, France Received 2025 May 12; revised 2025 July 16; accepted 2025 July 26; published 2025 August 29

Abstract

We present the discovery of a peculiar X-ray transient, EP241021a, by the Einstein Probe (EP) mission and the results from multiwavelength follow-up observations. The transient was first detected with the Wide-field X-ray Telescope as an intense flare lasting for ~ 100 s, reaching a luminosity of $L_{0.5-4~\rm keV} \approx 10^{48}\,\rm erg\,s^{-1}$. Further observations with EP's Follow-up X-ray Telescope reveal a huge drop in the X-ray flux by a factor of >1000 within 1.5 days. After maintaining a nearly plateau phase for ~ 7 days, the X-ray flux decreases $\propto t^{-1.2}$ over a period of ~30 days, followed by a sudden decrease to an undetectable level by EP and XMM-Newton, making it the longest afterglow emission detected among known fast X-ray transients. Bright counterparts at optical and radio wavelengths were also detected, with high peak luminosities in excess of 10^{44} erg s⁻¹ and 10^{41} erg s⁻¹ respectively. In addition, EP241021a exhibits a nonthermal X-ray spectrum, red optical color, X-ray and optical rebrightenings in the light curves, and fast radio spectral evolution, suggesting that relativistic jets may have been launched. We discuss the possible origins of EP241021a, including a choked jet with supernova shock breakout, a merger-triggered magnetar, a highly structured jet, and a repeating partial tidal disruption event involving an intermediate-mass black hole, but none can perfectly explain the multiwavelength properties. EP241021a may represent a new type of X-ray transient with month-duration evolution timescales; future EP detections and follow-up observations of similar systems will provide statistical samples to understand the underlying mechanisms at work.

Unified Astronomy Thesaurus concepts: X-ray transient sources (1852); Relativistic jets (1390); Tidal disruption (1696); Gamma-ray bursts (629); Black holes (162)

1. Introduction

In the past decade, a few tens of extragalactic fast X-ray transients (EFXTs) have been discovered with X-ray missions such as Swift, Chandra, and XMM-Newton, either from serendipitous observations or through target searches of archival data (e.g., A. M. Soderberg et al. 2008; P. G. Jonker et al. 2013; A. Glennie et al. 2015; F. E. Bauer et al. 2017; D. Alp & J. Larsson 2020; D. Lin et al. 2022; J. Quirola-Vásquez et al. 2022, 2023; D. Eappachen et al. 2023). These EFXTs are characterized by intense bursts of soft X-ray emission lasting tens to thousands of seconds with a wide range of luminosities, the nature of which remains enigmatic. Several possibilities have been invoked as the origins of EFXTs, including supernova shock breakout (SBO; A. M. Soderberg et al. 2008; D. Alp & J. Larsson 2020), long gamma-ray bursts (GRBs; F. E. Bauer et al. 2017), magnetars after binary neutron star mergers (D. Lin et al. 2022; J. Quirola-Vásquez et al. 2024), and stellar tidal disruption events (TDEs) involving an intermediate-mass black hole (IMBH; P. G. Jonker et al. 2013; Z.-K. Peng et al. 2019; R.-F. Shen 2019). On the other hand, EFXTs may represent a new and heterogeneous class of transient phenomena not well explained by any single model. Owing to the lack of prompt multiwavelength follow-up observations in previous studies, it is challenging to explore and distinguish these different mechanisms in detail.

Following its successful launch on 2024 January 9, the Einstein Probe (EP; also known as the Tianguan telescope) has started monitoring the sky in the soft X-ray regime (W. Yuan et al. 2025), ⁴⁶ opening a new avenue to characterize and study EFXTs. Operating in the 0.4–5 keV band, the Wide-field X-ray Telescope (WXT) on board EP has a large instantaneous field of view (~3600 deg²) and is capable of surveying the available night

Original content from this work may be used under the terms of the Creative Commons Attribution 4.0 licence. Any further distribution of this work must maintain attribution to the author(s) and the title of the work, journal citation and DOI.

sky several times per day. EP also carries an X-ray telescope (FXT) in the $0.3{\text -}10\,\text{keV}$ range, which has a larger effective area to perform follow-up observations and provide more precise localization of new transients triggered by WXT. The prompt follow-up FXT observations are capable of determining the temporal evolution of the afterglow X-ray emission (down to a typical sensitivity of $\sim 10^{-14}\,\text{erg}\,\text{cm}^{-2}\,\text{s}^{-1}$)—specifically the duration, light-curve shape, and spectral evolution, which are crucial to understanding the origin of FEXTs.

In its first year of scientific operations, EP/WXT has detected dozens of EFXTs in real time, most of which have received rapid follow-up observations at optical and radio bands. Analyzing the multiwavelength properties has revealed diversity in transient types and progenitor systems. A number of the EFXTs detected by EP have turned out to be GRBs, such as EP240219a (Y.-H. I. Yin et al. 2024), EP240315a (A. J. Levan et al. 2024; Y. Liu et al. 2025; R. Ricci et al. 2025), and EP240801a (S.-Q. Jiang et al. 2025). A few of the EP EFXTs have also been observed to show clear associations with broad-lined Type Ic supernovae (SNe Ic-BL) but without high-energy γ -ray counterparts, including EP240414a (S. Srivastav et al. 2025; H. Sun et al. 2025; J. N. D. van Dalen et al. 2025), EP250108a (R. A. J. Eyles-Ferris et al. 2025; W. X. Li et al. 2025; J. C. Rastinejad et al. 2025; G. P. Srinivasaragavan et al. 2025), and EP250304a (L. Izzo et al. 2025), which could be explained by a jet-forming supernova trapped in a dense envelope. It has also been suggested that they are linked to luminous fast blue optical transients owing to the detection of a delayed optical bump with a fast rise time, although it is not as blue (J. N. D. van Dalen et al. 2025).

In addition, EP has discovered a new type of X-ray transient with an intermediate evolutionary timescale. One of the most intriguing EFXTs is EP240408a, which was characterized by a postflare plateau lasting for ~4 days in the X-ray light curve, followed by a steep decay to an undetectable level about 10 days after the initial detection (W. Zhang et al. 2025). No optical, near-infrared, or radio counterparts were detected, making EP240408a's temporal properties inconsistent with

https://ep.bao.ac.cn/ep/

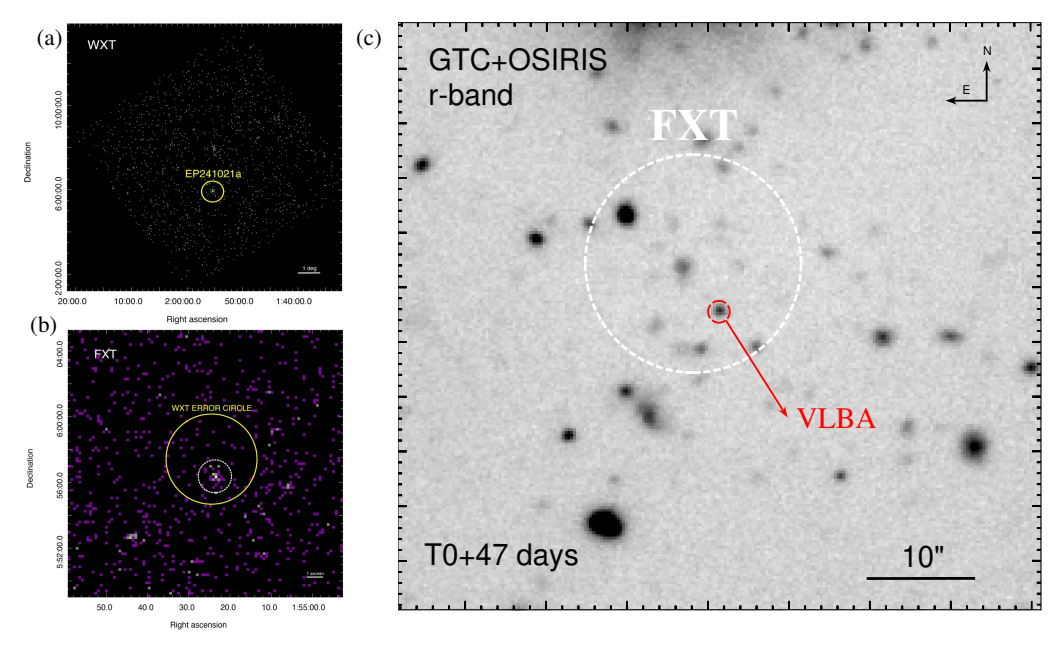


Figure 1. Multiwavelength images of EP241021a. (a) The image of EP241021a detected in one of the WXT CMOS detectors. (b) The image of EP241021a taken by one of the follow-up FXT observations. The white circle represents the center of the X-ray source localized by FXT, with a radius of 1', while the yellow circle shows the localization of WXT with an error circle of 3'. (c) The GTC r-band image observed on 2024 December 7, in which the optical counterpart was found within the FXT error circle (radius $\sim 10''$; dashed white circle). The radio position obtained by VLBA is marked by the small red circle, which can localize the optical counterpart with a positional uncertainty of ~ 1 mas.

any of the transient types known so far. Unfortunately, spectroscopic observations are not sensitive enough to confirm its redshift, preventing further investigations of the nature of EP240408a, although an exotic GRB or an abnormal jetted TDE was suggested (B. O'Connor et al. 2025).

In this Letter, we report the discovery of a peculiar EP X-ray transient, EP241021a, which exhibits long-lasting X-ray emission for more than 1 month, making it a possible EFXT with the longest evolutionary timescale ever observed. Shortly after the trigger, it was detected by follow-up observations at optical and radio bands. Optical spectroscopy reveals that the redshift of EP241021a is z = 0.748, based on the detection of narrow emission and absorption lines from the faint host galaxy. The multiwavelength observations and data reduction are described in Section 2. In Section 3, we present the detailed analysis of X-ray spectral and variability properties and the modeling of the radio flux and the evolution of the spectral energy distribution (SED). A discussion of possible interpretations for EP241021a is given in Section 4. We summarize the results in Section 5. We adopt a cosmology of $\Omega_M = 0.3$, $\Omega_{\Lambda} = 0.7$, and $H_0 =$ 70 km s⁻¹ Mpc⁻¹ when computing luminosity distances.

2. Observations

2.1. X-Ray Trigger and Observations

2.1.1. EP/WXT

The source EP241021a was initially detected by CMOS detector 10 of the EP/WXT (H. Cheng et al. 2025) during the observation conducted on 2024 October 21 between 04:51:21 and 05:10:39 UTC (J. W. Hu et al. 2024). Data reduction was performed using the <code>wxtpipeline</code> software tool (version 0.1.0). The WXT image in which EP241021a is detected ($\alpha=01^{\rm h}55^{\rm m}24.48$, $\delta=+05^{\circ}57'25.29$, J2000, with an uncertainty of 2.4) is shown in Figure 1(a). The light curve exhibits a significant flux increase from EP241021a that started

at 05:07:56 UTC and lasted $\sim 100 \, \mathrm{s}$ (Figure 2), with a time-averaged X-ray flux of $3.31^{+1.26}_{-0.86} \times 10^{-10} \, \mathrm{erg \, cm^{-2} \, s^{-1}}$ in the 0.5–4.0 keV band, corresponding to an isotropic-equivalent luminosity as high as $8.5 \times 10^{47} \, \mathrm{erg \, s^{-1}}$ at z = 0.748. The transient has a relatively hard X-ray spectrum that can be fitted by a power law with photon index $1.8^{+0.57}_{-0.54}$. We will refer to the time of the EP/WXT trigger as T_0 (MJD = 60604.214) for the phases (in days) of multiwavelength follow-up observations.

2.1.2. EP/FXT

Following the initial detection of EP241021a by WXT, an observation was performed with the FXT on board EP about 36.96 hr later. The exposure time was 3024 s, during which a previously uncataloged source was detected within the WXT's error circle, at J2000 coordinates $\alpha=01^{\rm h}55^{\rm m}23^{\rm s}.59$, $\delta=+05^{\circ}56'22.''20$ with an uncertainty of 10 (Y. Wang et al. 2024). Subsequent monitoring of EP241021a continued until 2025 January 8, consisting of a total of 12 observations (Table 1). The FXT was configured in full-frame mode in all the observations. The data were reduced using the fxtchain tool in the FXT Data Analysis Software. Detailed analysis of the X-ray spectra and light curve will be presented in Sections 3.1 and 3.2, respectively.

2.1.3. XMM-Newton

To fully constrain the late-time decay of EP241021a, we also obtained a target-of-opportunity observation with XMM-Newton (ObsID 0954190901; PI: Eyles-Ferris). This was performed on 2025 January 18, ~90 days after the first detection of EP241021a. We obtained the resulting Pipeline Processing System (PPS) files from the XMM-Newton Science Archive.⁴⁷ After filtering for background flares, exposure

⁴⁷ https://www.cosmos.esa.int/web/xmm-newton/xsa

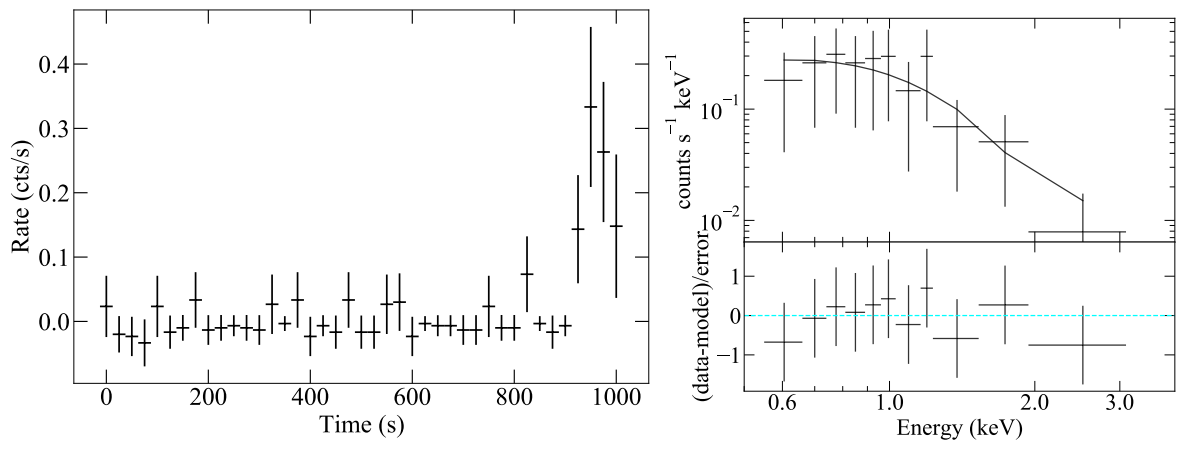


Figure 2. Left: the EP/WXT light curve of the count rate in the 0.5–4 keV band, in which an intense flare lasting \sim 91.9 s was observed. Right: the WXT X-ray spectrum during the flare period, which can be described by an absorbed single power-law model with photon index $\Gamma = 1.8^{+0.57}_{-0.54}$.

Table 1
Summary of X-Ray Observations Obtained from EP and XMM-Newton

1013				$(\text{erg s}^{-1} \text{ cm}^{-2})$	
	2024-10-21 04:51:25		5	$6.03^{+0.42}_{-0.19} \times 10^{-10}$	$1.80^{+0.57}_{-0.54}$
3024	2024-10-22 17:43:00	1.52	5	$2.19^{+0.32}_{-0.28} \times 10^{-13}$	1.83 ± 0.08
6044	2024-10-23 17:46:00	2.52	5	$2.00^{+0.19}_{-0.18} \times 10^{-13}$	•••
6037	2024-10-24 19:25:00	3.59	5	$1.45^{+0.18}_{-0.16} \times 10^{-13}$	
8559	2024-10-25 17:51:00	4.52	5	$1.41^{+0.14}_{-0.15} \times 10^{-13}$	
6122	2024-10-27 14:47:00	6.39	5	$1.66^{+0.20}_{-0.18} \times 10^{-13}$	
5575	2024-10-29 08:28:00	8.13	5	$2.09^{+0.25}_{-0.18} \times 10^{-13}$	
2093	2024-11-02 15:04:00	12.41	5	$0.91^{+0.26}_{-0.22} \times 10^{-13}$	
6175	2024-11-04 07:08:00	14.08	5	$0.79^{+0.14}_{-0.13} \times 10^{-13}$	
4791	2024-11-07 12:04:00	17.28	5	$0.87^{+0.18}_{-0.15} \times 10^{-13}$	
5966	2024-11-20 15:41:00	30.43	5	$0.47^{+0.13}_{-0.11} \times 10^{-13}$	
8943	2024-11-30 19:13:00	40.58	5	$0.31^{+0.10}_{-0.09} \times 10^{-13}$	
8706	2025-01-08 10:36:19	79.22		$<1.82\times10^{-14}$	
				15	
_	6044 6037 8559 6122 5575 2093 6175 4791 5966 8943	6044 2024-10-23 17:46:00 6037 2024-10-24 19:25:00 8559 2024-10-25 17:51:00 6122 2024-10-27 14:47:00 5575 2024-10-29 08:28:00 2093 2024-11-02 15:04:00 6175 2024-11-04 07:08:00 4791 2024-11-07 12:04:00 5966 2024-11-20 15:41:00 8943 2024-11-30 19:13:00 8706 2025-01-08 10:36:19	6044 2024-10-23 17:46:00 2.52 6037 2024-10-24 19:25:00 3.59 8559 2024-10-25 17:51:00 4.52 6122 2024-10-27 14:47:00 6.39 5575 2024-10-29 08:28:00 8.13 2093 2024-11-02 15:04:00 12.41 6175 2024-11-04 07:08:00 14.08 4791 2024-11-07 12:04:00 17.28 5966 2024-11-20 15:41:00 30.43 8943 2024-11-30 19:13:00 40.58 8706 2025-01-08 10:36:19 79.22	6044 2024-10-23 17:46:00 2.52 5 6037 2024-10-24 19:25:00 3.59 5 8559 2024-10-25 17:51:00 4.52 5 6122 2024-10-27 14:47:00 6.39 5 5575 2024-10-29 08:28:00 8.13 5 2093 2024-11-02 15:04:00 12.41 5 6175 2024-11-04 07:08:00 14.08 5 4791 2024-11-07 12:04:00 17.28 5 5966 2024-11-20 15:41:00 30.43 5 8943 2024-11-30 19:13:00 40.58 5 8706 2025-01-08 10:36:19 79.22	$\begin{array}{cccccccccccccccccccccccccccccccccccc$

Notes.

times were 38.2, 39.9, and 30.7 ks with the EPIC MOS1, MOS2, and pn detectors, respectively.

No source was detected at the position of EP241021a in any of the EPIC instruments. To derive the flux upper limits, we employed the method of R. P. Kraft et al. (1991) using a circular aperture of radius $10^{\prime\prime}$ centered on the source position. We estimated the background using a $60^{\prime\prime}$ radius aperture placed on the same chip as the source position and applied the PPS exposure maps to correct for vignetting. This was repeated for all three detectors, finding that MOS2 gives the deepest limit. We then converted the $0.2\text{--}12\,\text{keV}$ count rate to $0.3\text{--}10\,\text{keV}$ flux using Pimms v4.15 and a photon index of 1.83. The resulting unabsorbed flux upper limit is $<2.83\times10^{-15}\,\text{erg}\,\text{s}^{-1}\,\text{cm}^{-2}$ (at a 3σ confidence level).

2.2. Nondetections from Gamma-Ray Observations

There was no Fermi-Gamma-ray Burst Monitor (GBM) onboard trigger of EP241021a. An automated blind search for short GRBs below the onboard triggering threshold of Fermi-GBM also identified no counterpart candidates. The GBM targeted search for GRB-like signals was run from 30 s before the EP trigger time until 300 s after, but again, no signal was identified (E. Burns et al. 2024; GCN 37855). Konus–Wind (KW) was observing the position of EP241021a (D. Svinkin et al. 2024) for 1000 s before and after the trigger time and did not detect the source, with an upper limit (90% confidence level) for the 20–1500 keV peak flux of 2.5×10^{-7} erg cm⁻² s⁻¹ for a typical long GRB spectrum. This is an order of magnitude lower than the peak flux of long GRBs observed by KW (A. Tsvetkova

^a The spectrum during the 91.9 s flare is extracted and fitted at 0.5-4 keV, while the flux at 0.3-10 keV is reported based on the best-fit spectral model.

^b EP241021a was only detected by FXT-B.

^c EP241021a was not detected, and the corresponding 3σ upper limits on flux are given.

et al. 2017). Therefore, EP241021a was not detected by any high-energy gamma-ray observations and appears to fall below the lower end of the gamma-ray flux distribution of cosmological GRBs (M. Yadav et al. 2025).

2.3. Optical Photometry

The optical counterpart of EP241021a was first reported by the Nordic Optical Telescope (NOT) equipped with the Alhambra Faint Object Spectrograph and Camera at coordinates $\alpha = 01^{\rm h}55^{\rm m}23^{\rm s}41$, $\delta = +05^{\circ}56'18''.01$ with an uncertainty of 0.5 (S. Y. Fu et al. 2024b). This result was confirmed by earlier observations of the Thai Robotic Telescope network located at Fresno, California, USA (TRT-SRO; S. Y. Fu et al. 2024a), the 0.76 m Katzman Automatic Imaging Telescope (KAIT; A. V. Filippenko et al. 2001) located at Lick Observatory (W. Zheng et al. 2024b), and the Liverpool Telescope (LT) located at the Observatorio del Roque de los Muchachos, La Palma, Spain (A. Kumar et al. 2024; W. X. Li et al. 2024). After the first detection of the optical counterpart, several optical photometry follow-up campaigns were carried out, such as NOT; the Thai Robotic Telescope network located at New South Wales, Australia (TRT-SBO); the 50 cm A and 100 cm C telescopes of the JinShan project, located at Altay, Xinjiang, China (ALT-50A and ALT-100C); the Half-Meter-Telescope (HMT) located at Nanshan, Xinjiang, China; the 1.5 m telescope at Observatorio de Sierra Nevada, Spain (OSN); LT; the Gran Telescopio Canarias (GTC) located at Roque de los Muchachos Observatory, La Palma, Spain; LCO; and the 1.6 m Multi-channel Photometric Survey Telescope (Mephisto) located at Lijiang Observatory of Yunnan Astronomical Observatories, Chinese Academy of Sciences, and operated by the South-Western Institute for Astronomy Research, Yunnan University (Y. Pan et al. 2024).

The 1.6 m Mephisto observed EP241021a on 2024 October 29 in the u_m , v_m , g_m , r_m , i_m , and z_m bands, with two frames of 300 s exposures in each band. After stacking, the source was detected in the v_m and r_m bands. Follow-up observations in the v_m , r_m , and z_m bands were conducted on October 30, October 31, November 3, and November 4. Except for November 4 (one exposure per band), three exposures were obtained each night. Stacked images from November 3 show marginal detections in all three bands, while clear detections on the other nights were limited to the v_m and r_m bands. There was no detection on November 4. The Mephisto data reduction and calibration were performed following the method discussed in X. Chen et al. (2024).

For the images of NOT, Nanshan-HMT, and ALT-50A/100C, the data were processed using standard procedures with IRAF v2.16 (D. Tody 1986), including bias subtraction, flat-fielding, and image combination. Aperture photometry was conducted on the stacked frames, and the resulting flux was calibrated by nearby Pan-STARRS1 field stars (K. C. Chambers et al. 2016). For the LT images and the LCO images obtained in the program IAC2024B-004, we performed point-spread function photometry with the autophot package (S. J. Brennan & M. Fraser 2022), using stars in the Sloan Digital Sky Survey catalog for photometric calibration. The log of photometric observations and results is listed in Table A1 of Appendix A. Figure 3 displays the r-band light curve and r - z color evolution of EP241021a.

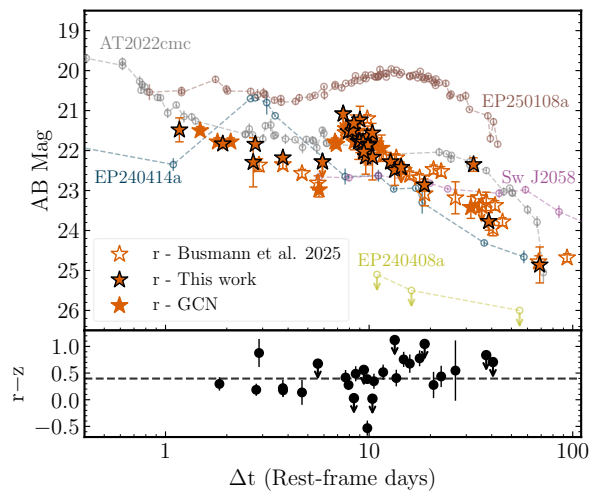


Figure 3. Optical (r-band) light curve of EP241021a. The photometric data are taken from our own observations (Section 2.3) and those reported in GCN Circulars and M. Busmann et al. (2025). Note that the flux excess observed by SVOM/VT (at $\Delta t \approx 18.6$ days) is due to the use of a broader r-band filter and hence should be treated with caution. For comparison, we present the r light curves of EP240414a (J. N. D. van Dalen et al. 2025) and EP250108a (W. X. Li et al. 2025)—the two EFXTs that are associated with SNe Ic-BL—as well as jetted TDEs Sw J2058 (S. B. Cenko et al. 2012) and AT 2022cmc (I. Andreoni et al. 2022). The peculiar EFXT EP240408a with an intermediate timescale but without an optical counterpart (down to 26 mag) is also plotted for comparison, assuming it is at z=0.5 (B. O'Connor et al. 2025; W. Zhang et al. 2025). The lower panel shows the r-z color evolution of EP241021a as a function of time. It is clear that the color is persistently red up to at least \sim 30 rest-frame days since discovery.

2.4. Optical Spectroscopy

We acquired long-slit spectroscopy of EP241021a with OSIRIS+ on the GTC on 2024 October 23 and 2024 October 29 (I. Pérez-Fournon et al. 2024), each with an exposure time of 1800 s. The R500R grism was used, corresponding to a wavelength coverage of 4800–10000 Å and a spectral resolution of $R \approx 500$. The data were reduced with the pypeit package (J. Prochaska et al. 2020) and flux calibrated with standard stars observed on the same night.

EP241021a was observed with the Low Resolution Imaging Spectrometer (J. B. Oke et al. 1995) on the Keck I 10 m telescope at the W. M. Keck Observatory on 2024 October 30 (W. Zheng et al. 2024a). The exposure time was $2 \times 1200 \, \mathrm{s}$ with the 600/4000 grism on the blue side ($R \approx 1100; \sim 3000-5600 \, \mathrm{A}$) and (simultaneously) the 400/8500 grating on the red side ($R \approx 1100; \sim 5400-9500 \, \mathrm{A}$). The spectrum was acquired with the 1'' wide slit oriented at or near the parallactic angle to minimize slit losses caused by atmospheric dispersion (A. V. Filippenko 1982). Data were processed using the LPipe (D. A. Perley 2019) data-reduction pipeline. The spectrum was flux calibrated using observations of appropriate spectrophotometric standard stars observed on the same night, at similar air masses, and with an identical instrument configuration.

As shown in Figure 4, the continuum of the Keck spectrum can be well fitted with a power law, $f_{\lambda} \propto \lambda^{-0.34}$. We clearly detect narrow emission lines of [O II] $\lambda 3727$, H β , and [O III] $\lambda \lambda 4959$, 5007 at a common redshift of z=0.7478, which likely originate from the host galaxy. We also detect an absorption-line system containing the Mg II $\lambda \lambda 2796$, 2803 doublet and Fe II lines at a similar redshift, making the redshift more reliable. The [O III] $\lambda 5007$ and [O II] $\lambda 3727$ lines

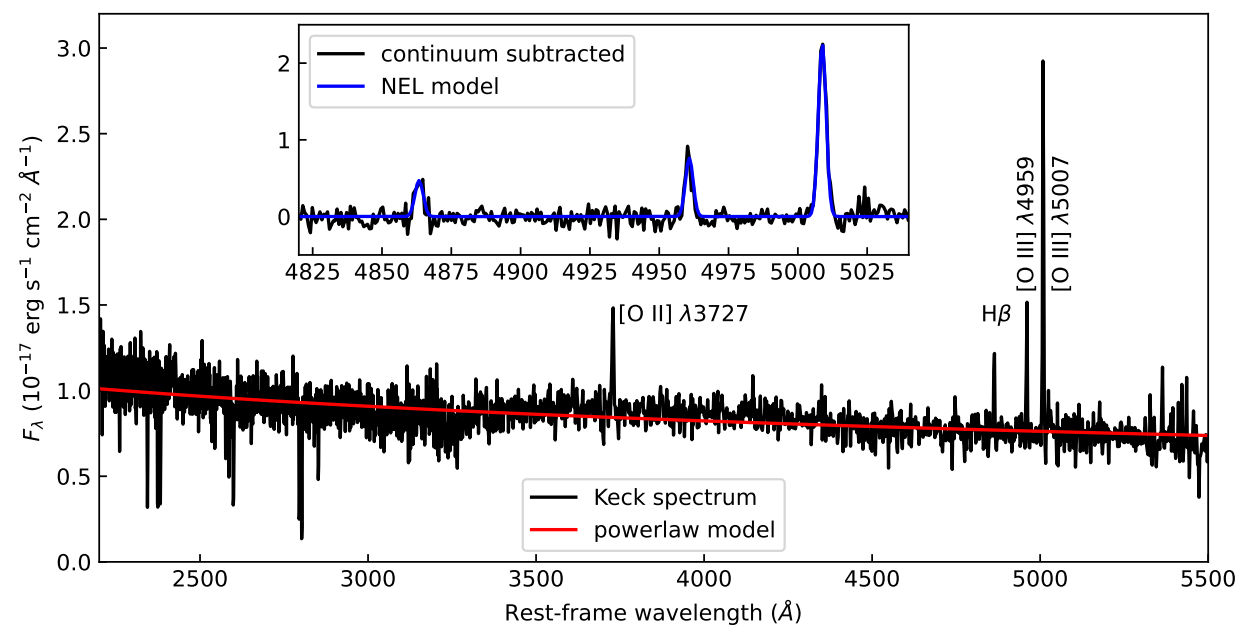


Figure 4. Keck spectrum of EP241021a taken on 2024 October 30 and the power-law model that can describe the continuum likely dominated by the transient. Wavelengths were converted into the rest frame according to the redshift z = 0.7478, which was obtained from the labeled narrow emission lines. We show in the inset the single Gaussian models that fit the H β and [O III] emission lines.

have luminosities of 3.6 \pm 0.1 \times 10⁴¹ and 1.7 \pm $0.2 \times 10^{41} \, \mathrm{erg \, s^{-1}}$, respectively. The measured full width at half-maximum (FWHM) intensity of [O III] is $200 \pm 6 \,\mathrm{km \, s}^{-1}$, consistent with the line-spread function of \sim 210 km s⁻¹ (measured using night-sky emission lines), indicating that the emission lines are narrow and unresolved. The line intensity ratio $[O III]/H\beta = 4.4 \pm 0.7$ indicates that the emission lines could be produced by either star formation or an active galactic nucleus (AGN; L. J. Kewley et al. 2006). No [Ne V] λ 3426 or [Ne III] $\lambda 3869$ are detected, and the intensity ratios [Ne III]/ [O II] < 0.17 and $[O III]/[O II] = 2.15 \pm 0.19$ are consistent with star-forming galaxies in the diagnostic diagram of L. M. Feuillet et al. (2024). Thus, the host is more likely to be a star-forming galaxy than an AGN. If so, the [O II] luminosity corresponds to a star formation rate of $2.4 \, M_{\odot} \, \text{yr}^{-1}$ according to the relation of R. C. Kennicutt (1998). While narrow emission lines such as [OIII], $H\beta$, and [OII] were detected in the GTC spectrum as well, confirming that EP241021a is at z = 0.7478, the signal-to-noise ratios (S/ Ns) are too low for meaningful spectral fittings (Figure A1 in Appendix A). Therefore, we report only the spectral fitting results from the Keck data.

2.5. Radio Observations

2.5.1. Very Large Array

While EP241021a was not detected by e-MERLIN on 2024 October 24 (G. Gianfagna et al. 2024), 3 days after discovery, a radio brightening was identified in both Australia Telescope Compact Array (ATCA) and AMI-LA observations on 2024 October 29–30 (F. Carotenuto et al. 2024; R. Ricci et al. 2024) with a radio luminosity at 5 GHz of \gtrsim 5 × 10⁴⁰ erg s⁻¹. To further study the radio properties, we triggered two-epoch Very Large Array (VLA) observations through a Director's Discretionary Time (DDT) program (project code VLA/24B-487) at central frequencies of 6 GHz (C band), 10 GHz (X

band), and 15 GHz (*Ku* band). The VLA observations were carried out 98 and 115 days after discovery.

Data were reduced using the Common Astronomy Software Applications (CASA, version 6.6.1; J. P. McMullin et al. 2007) and the standard VLA calibration pipeline (version 2024.1.1). Where the S/N allowed, we enhanced the frequency resolution by splitting the measurement set from groups of the spectral windows. We reran the pipeline after manually inspecting and additional flagging. The calibrated data were imaged using the CLEAN algorithm with Briggs weighting and a ROBUST parameter of 0, which helps to reduce side lobes and achieve good sensitivity. EP241021a was clearly detected in all observations. We used the IMFIT task in CASA to fit the radio emission with a two-dimensional elliptical Gaussian model to determine the position, integrated flux density, and peak flux density. The radio emission at all bands is unresolved, and no extended emission is detected. For consistency, only peak flux densities are used in our following analysis. The VLA observation log and flux-density measurements are presented in Table 2.

We also searched for radio emission at 3 GHz using the archival data from the Very Large Array Sky Survey (M. Lacy et al. 2020) but found that EP241021a remains undetected over its three-epoch observations between 2017 October and 2023 March, with a 5σ upper limit in the peak flux of \sim 0.8 mJy beam⁻¹.

2.5.2. MeerKAT

We conducted multifrequency radio observations with the MeerKAT telescope over two epochs (project code DDT-20250123-XS-01). The first-epoch observations were performed in the S0 and S4 bands (centered at 2.2 GHz and 3.1 GHz, respectively), while the *L*-band observations (with central frequency 1.3 GHz) were included in the second epoch. The MeerKAT observations were observed quasi-simultaneously as VLA to measure the broadband SED and its evolution. We used the "4K" wideband coarse mode to ensure

Table 2Summary of the Radio Observations of EP241021a

Observatory	Project	ν (GHz)	UTC Date	Phase (days)	$F_{ u}$ (mJy)
ATCA	CX585	5.0	2024 Oct 29	8	0.350 ± 0.029
		5.5	2024 Oct 29	8	0.382 ± 0.024
		6.0	2024 Oct 29	8	0.407 ± 0.029
		8.5	2024 Oct 29	8	0.434 ± 0.028
		9.0	2024 Oct 29	8	0.453 ± 0.026
		9.5	2024 Oct 29	8	0.467 ± 0.028
VLBA	BS346	6.2	2024 Nov 28	37	0.774 ± 0.072
		8.4	2024 Nov 30	39	0.762 ± 0.081
VLA	24B-487	5.0	2025 Jan 28	98	0.544 ± 0.038
		7.0	2025 Jan 28	98	0.374 ± 0.038
		15.0	2025 Jan 28	98	0.110 ± 0.020
		10.0	2025 Feb 14	115	0.225 ± 0.074
		6.0	2025 Feb 21	122	0.319 ± 0.025
MeerKAT	DDT-20250123-XS-01	2.2	2025 Jan 29	99	0.522 ± 0.027
		3.1	2025 Jan 29	99	0.478 ± 0.025
		1.3	2025 Feb 15	116	0.375 ± 0.020
		2.2	2025 Feb 16	117	0.367 ± 0.020
		3.1	2025 Feb 16	117	0.413 ± 0.022

high sensitivity. For the first epoch, the total time was \sim 1.9 hr in each band, of which 1.5 hr were spent on the source and 0.4 hr on the flux and phase calibrators (J0408–6545 and J0149 +0555), resulting in an rms of \sim 10 μ Jy. A shorter on-source exposure (0.7 hr) in each band was used for the second-epoch observations, yielding a larger rms of \sim 20 μ Jy.

We reduced the MeerKAT data using the OxKAT software (I. Heywood 2020), and the final images were cleaned with the WSClean algorithm (A. R. Offringa & O. Smirnov 2017). We then measured the integrated and peak flux in CASA, following the same procedures described above. The source is clearly detected in all three bands. The ratio of the integrated flux to the peak flux is in the range of 0.92–1.06, with a median value of 0.99, suggesting that most, if not all, of the radio emission is unresolved, consistent with observations from other telescopes, although the spatial resolution is very different. The flux densities obtained from MeerKAT observations are listed in Table 2.

2.5.3. Very Long Baseline Array

We carried out Very Long Baseline Array (VLBA) observations at the location of EP241021a on 2024 November 28 at 6.186 GHz and 2024 November 30 at 8.368 GHz with its 10 antennas (project code BS346). The observing frequency was centered at 6.186 GHz in the C band and 8.368 GHz in the X band. The observation was performed in the phasereferencing mode to the nearby strong compact radio source J0149+0555. Phase-reference cycle times were 4.5 minutes, with 3.5 minutes on-target and 1.0 minutes for the phase calibrator. We also inserted several scans of the bright radio source 3C 84 for fringe and bandpass calibration with an integration time of 3.0 minutes for each scan. The resulting total on-source time on both bands is 5 hr. To achieve sufficiently high imaging sensitivity, we adopted the observational mode RDBE/DDC to use the largest recording rate of 2 Gbps, corresponding to a recording bandwidth of 256 MHz in each of the dual circular polarizations. We used the NRAO AIPS software to calibrate the amplitudes and phases of the

visibility data, following the standard procedure from the AIPS Cookbook. The calibrated data were imported into the Caltech DIFMAP package (M. C. Shepherd 1997) for imaging and model fitting. During imaging, we noted that the gain solutions were bad for the MK, SC, and HN antennas at 6.2 GHz and the HN antenna at 8.4 GHz. Therefore, we flagged data from these antennas.

VLBA detects a compact source in the final cleaned image, which has a deconvolved size of 3.77 mas \times 1.12 mas. To further investigate whether the source is resolved or not, we used the task Modelfit in DIFMAP to fit the radio emission but found no additional emission components in the residual map. Therefore, EP241021a remains compact and unresolved at the resolution of VLBA observations, with an upper limit on its size of <8.22 pc. The position of the radio source observed by VLBA is (J2000) $\alpha = 01^{\rm h}55^{\rm m}23^{\rm s}.4323$, $\delta = +05^{\circ}56'17.7'7978$. The VLBA observation log and flux-density measurements are presented in Table 2.

2.5.4. ATCA

EP241021a was observed with ATCA in the 16 cm and 4 cm bands. The observations were made in the 6A configuration on 2024 October 29 (R. Ricci et al. 2024; program ID CX585, GCN 37949) and were carried out with two 2 GHz wide intermediate frequencies (IFs) of 4.5–6.5 GHz (centered at 5.5 GHz) and 8–10 GHz (centered at 9 GHz). PKS B1934–638 was used as a bandpass and flux-density calibrator, and 0146 +056 was used as a complex-gain calibrator. Data reduction was carried out with the software *Miriad* (R. J. Sault et al. 1995), following standard procedures.

First, we performed the automatic radio frequency interference (RFI) flagging by using the task *pgflag* before calibration to reduce the influence of RFI. Second, standard calibration involved bandpass and flux-density calibration on PKS B1934–638 using the *Miriad* tasks *mfcal* and *gpcal*, and this was applied to the gain calibrator 0146+056. Time-

⁴⁸ http://www.aips.nrao.edu/cook.html

varying gains and polarization leakage calibration were done using the task *gpcal* on 0146+056, and these gains were transferred and applied to the target before imaging.

Imaging was performed using the tasks *invert*, *cgdisp*, *mfclean*, and *restor* to create six continuum images (three for each of the IFs). Images were made in Stokes *I*, with a Briggs visibility weighting robustness parameter of 0.5. Images were restored with a Gaussian synthesized beam of $27\rlap.21 \times 1\rlap.36$ with a position angle of -1.5^c *irc* for the 5.5 GHz image and $16\rlap.78 \times 0\rlap.83$ with a position angle of -1.5^c *irc* for the 9 GHz image. EP241021a was clearly detected in all bands; the radio emission is unresolved, and no extended emission is detected. The central region of the 5.5 GHz image has an rms noise level of $15.1~\mu Jy$ beam $^{-1}$, while the 9 GHz image has an rms noise level of $11.8~\mu Jy$ beam $^{-1}$. The flux density of the target was fitted by using the task *imfit*. The ATCA observation log and flux-density measurements are presented in Table 2.

3. Analysis and Results

3.1. X-Ray Spectra

We grouped the spectra to have at least 1 count in each bin so as to adopt the C-statistic for the spectral fits. The following spectral analysis was performed with the software BXA (J. Buchner et al. 2014), which connects the nested sampling algorithm UltraNest⁴⁹ (J. Buchner 2021) and integrates the conventional spectral fitting software XSPEC (version 12.14.1). For the EP/WXT spectral fittings, a simple absorbed power-law model provides an acceptable fit (Figure 2), yielding a best-fit photon index of $\Gamma = 1.8^{+0.57}_{-0.54}$. Given the limited spectral S/N for the EP/FXT data, we performed a joint fit of all the EP/FXT spectra in the 0.3-10 keV band using the data from epochs when EP241021a was detected; the photon indices were tied, and $N_{\rm H}$ was frozen at the Galactic value of $5 \times 10^{20} \, {\rm cm}^{-2}$. A single uniform prior is defined for each parameter, and the best-fit values with 68.3% uncertainty margins are given by the posterior distributions. The resulting photon index is 1.83 ± 0.08 , consistent with that obtained by WXT, suggesting marginal spectral evolution during the FXT observations. To secure the result, we used addspec 1.4.0 to stack the exposure-weighted X-ray spectra from the first six FXT observations that exhibit relatively small flux variations. The stacked spectrum can also be described by an absorbed power-law model with a photon index of 1.8 ± 0.1 , as shown in Figure 5 (left). We used this best-fit model to extrapolate the flux in the 0.3–10 keV band for all the EP/FXT data as well as those observed by XMM-Newton. For the last FXT observation, EP241021a was faint and not detected. Based on the aperture-photometry method (R. P. Kraft et al. 1991; A. Ruiz et al. 2022), we estimated the flux upper limit at a 3σ confidence level. All the X-ray flux measurements are shown in Table 1.

3.2. X-Ray Light Curve

During the 91.9 s flare period, EP/WXT collected a total of 26 photon counts from EP241021a, with no significant short-timescale features being discernible. EP241021a could not be distinctly separated from the background during nonflare intervals. Following the X-ray flare detected by EP/WXT, EP/FXT observed EP241021a between 1 and 79 days since

trigger. As shown in Figure 5 (right), the X-ray light curve exhibits a nearly plateau phase for the first 7 days, followed by a steep decline up to 79 days, after which EP241021a becomes undetectable by EP/FXT, with a 3σ upper limit on the flux of 1.82×10^{-14} erg cm⁻² s⁻¹. EP241021a remains undetected by more sensitive XMM-Newton observations at $t_0 + 89$ days, with a 3σ confidence upper limit on the flux of 2.83×10^{-15} erg cm⁻² s⁻¹ (Section 2.1.3).

To quantify the evolution of the X-ray emission, we first fitted a smoothed broken power law to the light curve in the rest frame (Appendix B), excluding the EP/WXT data. Although the model can describe the EP/FXT data, it seems to overpredict the flux if compared to the upper limit obtained by XMM-Newton, indicating a steep break in the light curve. Therefore, we included a third power law to take into account the steep flux break and found that it provides a statistically better fitting result over the previous broken power-law model, according to the Bayes factor of K = 4.12. Therefore, we favor the three piecewise power-law function as the model to describe the light-curve evolution. We used a Markov Chain Monte Carlo (MCMC) fitting technique to determine the bestfitting parameters and uncertainties (Appendix B). Based on this, we found a slope of $L_{\rm X} \propto t^{-0.28^{+0.17}_{-0.13}}$ for the plateau's decline, which breaks to $t^{-1.16^{+0.30}_{-1.11}}$ at a rest-frame time of $t_{\rm rest} = 6.1^{+8.58}_{-1.39}$ days post-trigger, followed by a steeper drop at $t_{\text{rest}} = 33.49^{+10.67}_{-9.72}$ days, with $t^{-9.64^{+6.92}_{-7.04}}$. We note that the powerlaw slope for the final drop phase in the luminosity evolution was poorly constrained, owing to the sparse temporal coverage in the light curve between the last EP/FXT detection and the late-time limit provided by XMM-Newton.

3.3. Radio Flux and SED Evolution

As mentioned in Section 2.5.1, a radio transient was detected ~ 8 days after the discovery of EP241021a. The radio luminosity at 5 GHz is as high as \gtrsim 5 \times 10⁴⁰ erg s⁻¹, comparable to jetted TDEs and long GRBs at similar evolution epochs (e.g., J. H. Gillanders et al. 2024). Combined with the detections of fast X-ray variability, a nonthermal X-ray spectrum (Section 2.1), and red optical color (Section 2.3), this indicates that a relativistic outflow may have been launched. Figure 6 shows the radio SED and its evolution over four epochs, which was constructed using the publicly available ATCA data (R. Ricci et al. 2024; GCN 37949), as well as our own data obtained with MeerKAT, VLA, and VLBA. Upon the radio detection, the SED peaks at \sim 10 GHz but exhibits a shift toward higher flux density through restframe 18 days. The joint MeerKAT and VLA observations, taken between 57 and 67 rest-frame days post-trigger, revealed that the peak of the SED shifts downward to \sim 2 GHz, with a flux of ~ 0.5 mJy.

To quantify the temporal evolution, we fit the SED with a synchrotron emission model in the context of a relativistic outflow expanding into the surrounding medium. The interaction of outflow with the surrounding medium leads to synchrotron emission owing to the acceleration of electrons and amplification of magnetic fields. This model has been widely used to explain the radio emission from GRBs (e.g., J. Granot & R. Sari 2002; J. Granot & A. J. van der Horst 2014) and TDEs (e.g., E. Berger et al. 2012; K. D. Alexander et al. 2016), as the basic framework is quite general.

Owing to the sparse sampling of the radio spectrum and the lack of high-frequency observations, we fit the radio spectrum

⁴⁹ https://johannesbuchner.github.io/UltraNest/

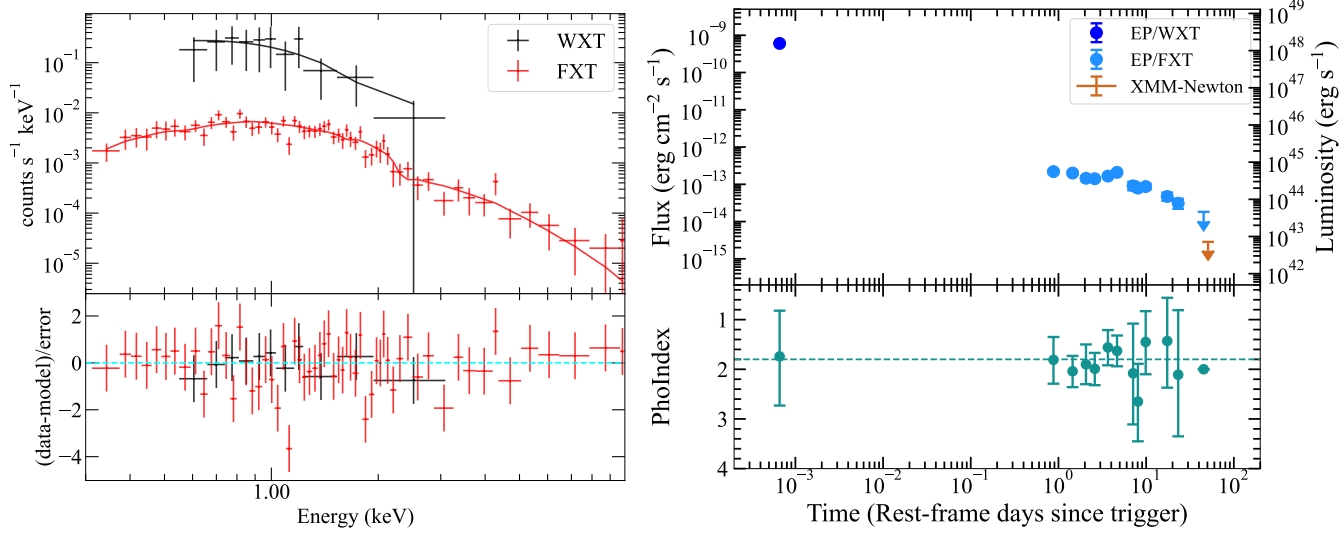


Figure 5. Left: the EP/FXT spectrum in the 0.3–10 keV band by stacking the first six observations in the plateau phase (total exposure \sim 35 ks). The photon index for the stacked EP/FXT spectrum is 1.8 ± 0.1 if fitted by an absorbed power law, consistent with that of EP/WXT. Note that the X-ray spectrum is relatively flat and consistent with nonthermal emission. Right: X-ray light curves of EP241021a observed by EP/WXT, EP/FXT, and XMM-Newton. The EP/FXT fluxes in the upper panel were obtained with the photon index tied during fitting. The lower panel shows the distribution of the photon index for the power-law component that was allowed to vary in the individual spectral fittings and is consistent with the value $\Gamma = 1.8$ within the errors. More details of modeling the light-curve evolution can be found in Appendix B.

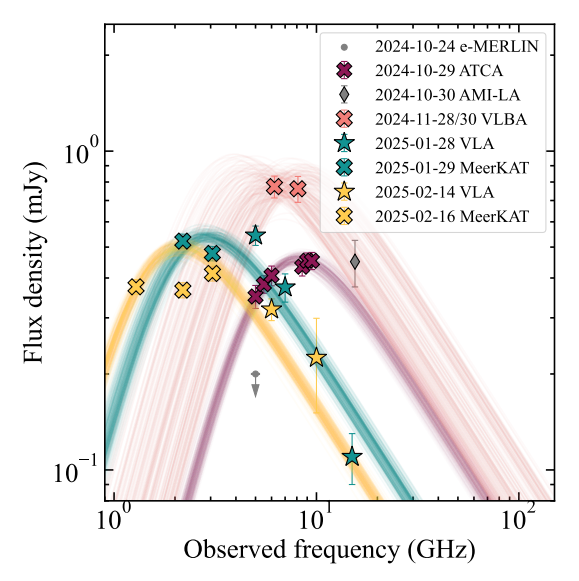


Figure 6. The radio SEDs over four epochs that have quasi-simultaneous observations at different frequencies. For nondetections, the corresponding 5σ upper limits on flux density are shown. The colored lines represent the best fit to each SED from our MCMC modeling, which are the model realizations on a basis of 200 random samples from the MCMC chains.

using the synchrotron spectrum 2 model described by J. Granot & R. Sari (2002), assuming $\nu_m \ll \nu_a$, where ν_m is the characteristic synchrotron frequency of the emitting electrons with the least energy and ν_a is the self-absorption frequency, and fixing the synchrotron energy index in the optically thin regime to p=3 (e.g., Y. Cendes et al. 2021). We use an MCMC fitting technique (python module emcee; D. Foreman-Mackey et al. 2013) to marginalize over the synchrotron model parameters to determine the best-fitting parameters and uncertainties. In Figure 6, we show the resulting SED models, which provide reasonable fits to the data. From the best-fitting SED models, we determine the peak flux density and frequency, $F_{\nu,p}$ and ν_p , respectively.

Using the inferred values of $F_{\nu,p}$ and ν_p , we can calculate the equipartition radius and energy in the relativistic regime assuming the outflow is viewed on-axis (R. Barniol Duran et al. 2013), which was derived as

$$R_{\rm eq} \approx (1.7 \times 10^{17} \text{ cm}) \left[\frac{F_{p,\,{
m mJy}}^{8/17} d_{L,28}^{16/17} \eta^{35/51}}{\nu_{p,10} (1+z)^{25/17}} \right] \frac{\Gamma^{10/17}}{f_A^{7/17} f_V^{1/17}},$$

$$E_{\rm eq} \approx (2.5 \times 10^{49} \ {\rm erg}) \left[\frac{F_{p,\,{\rm mJy}}^{20/17} d_{L,28}^{40/17} \eta^{15/17}}{\nu_{p,10} (1+z)^{37/17}} \right] \frac{f_V^{6/17}}{\Gamma^{26/17} f_A^{9/17}}.$$

Here f_V and f_A are geometric factors, $\eta=1$ for $\nu_m \ll \nu_a$, and Γ is the Lorentz factor of the outflow. Considering the exceptionally high X-ray and radio luminosity likely due to a strong beaming effect, we assume a narrow jet with a half-opening angle of $\theta_i=0.1<1/\Gamma$, such that $f_A=f_V=(\theta_i\Gamma)^2$.

To find the minimal energy using equipartition arguments, we need another equation that relates the time since the onset of the relativistic outflow t, the radius R, and the Lorentz factor (Γ) ,

$$t \approx \frac{R(1-\beta)(1+z)}{\beta c}$$

where β is the velocity of the outflow. The equipartition analysis suggests a modest Lorentz factor $\Gamma \approx 3$ and an equipartition energy $E_{\rm eq} \approx 10^{50}\,{\rm erg\,s^{-1}}$. Note that the total minimal energy will be increased by a factor of $(1+\epsilon_e^{-1})^{7/12}$ if considering that the hot protons carry a significant portion of the total energy (R. Barniol Duran & T. Piran 2013). Furthermore, if considering the case that we are away from equipartition, the estimate on the Lorentz factor is still valid. In this case, the total energy will be larger by a factor of $\sim 0.5 \epsilon_e^{-0.6} \epsilon_B^{-0.4}$ if $\epsilon_e + \epsilon_B < 1$, where ϵ_e and ϵ_B are the microphysical parameters, respectively the fractions of the total energy in electrons and magnetic field.

We note that the flux in the S0 band (2.2 GHz) observed by MeerKAT decreased from 0.51 to 0.39 mJy over 2 weeks, while the variability amplitude observed in other MeerKAT bands was not as significant as that in the S0 band. We consider whether the observed variability might be affected by interstellar scintillation (ISS). This process occurs when radio waves propagate through an inhomogeneous plasma in our Galaxy, which could cause intraday variability in some AGNs with compact radio emission (J. E. J. Lovell et al. 2003; B. J. Rickett 2007). The amount and timescale of radio variation caused by ISS depend on the Galactic electron column density along the line of sight (LOS) and the observing frequency. Using the NE2001 free electron density model developed by J. M. Cordes & T. J. W. Lazio (2002)⁵⁰ and the Galactic dispersion measure (DM),⁵¹ we find that, at the position of EP241021a, the transition frequency between the strong- and weak-scattering regime is $\nu_0 \approx 7.93$ GHz, and the angular size limit of the first Fresnel zone at the transition is $6.2 \,\mu as.$ Adopting the formalism of M. A. Walker (1998), we estimate that the level of frequency- and time-dependent random flux variations induced by ISS is from 59% at 3.1 GHz to 2.8 % at 15.0 GHz for EP241021a. When adding the ISSinduced flux variations to the measurement uncertainties, the radio SED fittings in the epoch II and III observations cannot converge. This is because the SED sampling is either too sparse or peaks at lower frequency, where the expected ISS effect is large. On the other hand, we find that while the ISS effect increases the uncertainty in the derived physical parameters for the epoch I and IV observations, it does not bias the above estimation of the Lorentz factor and total minimal energy of the outflow. Note that the ISS effect on the radio variability is also explored by M. Yadav et al. (2025), in which the size of the radio-emitting region can be constrained. By estimating the brightness temperature of the radio emission, M. Yadav et al. (2025) derived a lower limit for the Lorentz factor $\Gamma \gtrsim 5.5$ at $T_0 + 1.5$ days (T_0 is the time of the trigger), consistent with the value constrained by the SED fittings.

4. Discussion

Here we summarize the multiwavelength properties of EP241021a, highlighting the uniqueness in its temporal evolution.

- (1) EP241021a was triggered by EP/WXT and had a duration of $\sim \! 100 \, \mathrm{s}$, with a time-averaged X-ray flux (0.5–4 keV) of $3.31 \times 10^{-10} \, \mathrm{erg \, cm^{-2} \, s^{-1}}$, corresponding to an isotropic-equivalent energy of the prompt emission $E_{\mathrm{iso}} \approx 8.5 \times 10^{49} \, \mathrm{erg}$. The flare's X-ray spectrum is relatively hard with a photon index $\Gamma = 1.8^{+0.57}_{-0.54}$, likely associated with nonthermal emission.
- (2) An X-ray counterpart was detected by EP/FXT about 36.96 hr after the trigger, with a flux (0.3–10 keV) of $2.19 \times 10^{-13} \, \mathrm{erg \, cm^{-2} \, s^{-1}}$, implying a rapid flux decline by more than 3 orders of magnitude within about 1.5 days. During the phase from $T_0 + 1.5$ to 8 days, the evolution of the X-ray emission enters a nearly plateau phase, with a sign of late-time rebrightening. The FXT observations confirmed the hard X-ray

spectrum, with no significant spectral evolution. Then the X-ray emission shows a power-law decline with $t^{-1.2}$ over ~ 30 days, followed by rapidly dropping below detection.

- (3) Optical emission associated with EP241021a was detected within 1.8 days after the X-ray trigger, possibly related to the afterglow of the prompt X-ray emission. At $T_0 + 6$ days, an optical brightening was observed peaking at \sim -21.5 mag in the r band, with a fast rise time of only \sim 2 days. Such a fast timescale of the optical evolution and high peak luminosity resemble those of luminous fast blue optical transients (A. Y. Q. Ho et al. 2023). During the optical peak, Keck spectroscopy was performed, revealing narrow emission lines from the host galaxy and providing the redshift of EP241021a at z = 0.748. A late-time optical rebrightening appears at $T_0 + 20.7$ days, though it is not as significant and bright as the second one, with a peak of ~ -20.2 mag. EP241021a exhibits a persistent red color $(r - z \approx 0.4 \,\mathrm{mag})$ over a period of at least 40 days since discovery, which is unusual among known optical transients. There is a potential coincidence between the phases of optical and X-ray brightenings.
- (4) Follow-up radio observations reveal the appearance of the radio counterpart at $T_0+8.4\,\mathrm{days}$. Over the period of $\sim\!110\,\mathrm{days}$ of post-trigger radio observations, the peak flux density increases for the first month, followed by a decrease in the subsequent 2 months. During this time range, the self-absorption frequency decreases. The radio spectral luminosity is as high as $\sim\!10^{31}\,\mathrm{erg\,s^{-1}\,Hz^{-1}}$, comparable to that of long GRBs and jetted TDEs at similar evolution epochs. An equipartition analysis suggests that a relativistic outflow with a moderate bulk Lorentz factor ($\Gamma\approx3$) and a minimum energy of $10^{50}\,\mathrm{erg\,s^{-1}}$ may have been launched.

The X-ray, optical, and radio observations suggest that EP241021a is an extremely unusual transient, and multiple emission components might be required to account for its multiwavelength properties, such as various mechanisms to produce the rebrightening emission or episodic energy injections from multiple outflows. In the next section, we will explore the possible scenarios that could accommodate the multiwavelength behavior of EP241021a.

4.1. A Choked/Weak Jet and a Supernova SBO

Both the isotropic energy and the peak energy of the prompt emission are significantly lower than those of conventional long GRBs. While the luminosity of EP241021a falls into the range of low-luminosity GRBs, it stands as an outlier from the Amati-Yonetoku relation owing to its lower peak energy, similar to the EP EFXTs EP240414a and EP250108a, both of which are associated with SNe Ic-BL (W. X. Li et al. 2025; H. Sun et al. 2025). Together with the nondetection of highenergy gamma-ray emission, it has been proposed that a collapsar-driven low-energy jet choked in extended circumstellar material (CSM) can explain their multiwavelength properties (R. A. J. Eyles-Ferris et al. 2025; H. Hamidani et al. 2025). In this scenario, multiple emission components are invoked to account for the evolution in different phases, including the early-phase afterglow emission from the choked/ weak jet, the late-phase emission from an SN Ic-BL, and the middle rebrightening phase due to supernova SBO. In addition, the cocoon produced by the interaction of the jet with the dense CSM could contribute to the emission (H. Hamidani et al. 2025).

⁵⁰ https://pypi.org/project/pyne2001/

⁵¹ EP241021a has Galactic coordinates of $(l, b = 150^{\circ}.3520610, -53^{\circ}.4941773)$. We used the DM of 27.5 cm⁻³ pc for EP241021a, which was derived from the pulsar J0156+0402 $(l, b = 151^{\circ}.9997139, -55^{\circ}.1844179)$ in the ATNF Pulsar Catalog.

Generally speaking, no supernova-like features were identified in the late-time optical EP241021a (M. Busmann et al. 2025). However, such a negative supernova observation could just be due to the relatively large distance of the source. One cannot fully rule out that the second optical bump is produced by the breakout of the supernova shock from the CSM. In order to account for the fast evolution of the optical bump and its bolometric luminosity of $L_{\rm opt} \approx 10^{44}\,{\rm erg\,s^{-1}}$, the mass of the CSM would be required to be about $10\,M_{\odot}$, which spreads within a range of several thousand solar radii (D. K. Khatami & D. N. Kasen 2024). However, it could still be not easy to account for the large radius of the emitting photosphere, which can be constrained to

$$R_{\rm ph} = \left(\frac{L_{\rm p}}{4\pi\sigma_{\rm SB}T^4}\right)^{1/2}$$

$$\approx 3.8 \times 10^{15} \left(\frac{L_{\rm p}}{10^{44} \,{\rm erg \, s^{-1}}}\right)^{1/2} \left(\frac{T}{10^4 \,{\rm K}}\right)^{-2} {\rm cm}, \qquad (1)$$

where $\sigma_{\rm SB}$ is the Stefan–Boltzmann constant and the reference value of the blackbody temperature T is taken according to its relatively red color. Furthermore, the existence of the dense CSM could effectively hinder the propagation of the jet/cocoon and thus the generation of the afterglow emission. Finally, very different from EP240414a and EP250108a, EP241021a displays long-lasting X-ray afterglow emission ($\Delta T \approx 39$ days), with a flux brightening that appears to coincide with the optical bump. This X-ray brightening obviously cannot be contributed by the cooling cocoons or generated by a radiation-mediated shock propagating into the dense CSM (B. Margalit et al. 2022).

4.2. A Magnetar Engine and Its Possible Origin

Even if the rebrightening is not due to a supernova SBO, could it instead originate from another type of supernovarelated emission? Using the photospheric radius given in Equation (1) to represent the outer radius of the explosion ejecta, which can be correct when the ejecta are optically thick at early times, we can constrain the expansion velocity of the ejecta to be $v_{\rm ej} \approx 0.25c$. This value is obviously higher than the typical velocity of supernovae, which is no more than $\sim 0.1c$ (e.g., Y.-Q. Liu et al. 2017; C. Barbarino et al. 2021). Meanwhile, according to the prompt emission energy of $\sim 10^{50}$ erg and assuming a reference radiation efficiency of \sim 10%, we can further take the initial kinetic energy of the explosion ejecta to be $E_{\rm k} \approx 10^{51}$ erg, which is typical for both normal supernova explosions and compact binary mergers. Combining the estimates of v_{ej} and E_k , the mass of the ejecta can be calculated as $M_{\rm ej} \approx 0.02\,M_{\odot}$. Then, we can express the photon diffusion timescale of the expanding ejecta by

$$t_{\text{diff}} \approx \left(\frac{3\kappa_{\text{opt}} M_{\text{ej}}}{4\pi c \nu_{\text{ej}}}\right)^{1/2} \approx 6.5 \left(\frac{\kappa}{10 \text{ cm}^2 \text{ g}^{-1}}\right)^{1/2} \times \left(\frac{M_{\text{ej}}}{0.02 M_{\odot}}\right)^{1/2} \left(\frac{\nu_{\text{ej}}}{0.25 c}\right)^{-1/2} \text{ days}, \tag{2}$$

which indicates that a relatively high opacity ($\kappa_{\rm opt} \approx 10~{\rm cm^2~g^{-1}}$) would be invoked to match the observed peak time of the optical rebrightening.

The large speed, low mass, and high opacity of the ejecta point to EP241021a possibly originating from the merger of a binary neutron star or the collapse of a super-Chandrasekharmass white dwarf. In the former case, it is widely believed that an amount of lanthanides can be synthesized in the neutronrich ejecta, which can give a natural explanation for the ultrahigh opacity of $10-100\,\mathrm{cm^2\,g^{-1}}$ (D. Kasen et al. 2013). The low mass of the ejecta further indicates that the prompt emission energy of EP241021a, $\sim 10^{50}$ erg, cannot be provided by the decay of radioactive elements in the ejecta and instead requires a more powerful energy source. As widely suggested, such an extra energy supply can be provided naturally by the remnant compact object, which is most likely a millisecond magnetar (Y.-W. Yu et al. 2013; B. D. Metzger & A. L. Piro 2014; Y.-W. Yu et al. 2019a, 2019b). In this case, the magnetar not only enhances the optical thermal emission of the ejecta but also generates X-rays directly through its wind nebula emission. So, the X-ray bump associated with the optical transient can be explained by the leakage of the nebula emission from the ejecta (Y.-W. Yu et al. 2019a). For detailed modeling of EP241021a in this scenario, please see G.-L. Wu et al. (2025). In particular, if this millisecond magnetar is specifically formed from the accretion-induced collapse of a white dwarf, then the interaction between the magnetar and the residual companion star could further lead to intermittent energy injection into the ejecta. As a result, some postpeak light-curve bumps could be produced (J.-P. Zhu et al. 2024), just as observed in EP241021a.

In such magnetar engine cases, the $\sim 100\,\mathrm{s}$ bright X-ray emission detected by WXT may be attributed to the magnetar wind dissipation during the initial spin-down period (B. Zhang 2013; H. Sun et al. 2017; C. Chen et al. 2025). Gravitational-wave signals may accompany the event but are too faint to be detected with the current gravitational-wave detectors. The dissipation of the released spin-down energy could occur through magnetic reconnection that converts a Poynting flux to an ultrarelativistic wind, which is most likely detected from a viewing angle away from the central jet. Additionally, X-ray emission can be produced by the collision of this wind with the preceding jet or the CSM. In any case, similar to normal GRBs, we cannot rule out that the prompt X-ray emission is contributed by internal dissipation in the mildly relativistic jet.

4.3. A Structured GRB Jet

The general synchronous evolution of the optical and X-ray emission could also indicate that the multiwavelength brightenings are the result of the dynamical evolution of a structured jet, as observed in some GRBs (e.g., O. S. Salafia & G. Ghirlanda 2022). On the one hand, the jet could be radially structured, and its external shock can be continuously refreshed because of energy injection from the catching-up and more energized jet material (M. J. Rees & P. Mészáros 1998; Y. W. Yu et al. 2007; M. Busmann et al. 2025). However, in this scenario, it could not be easy to produce a flux jump of $\delta t/t \approx 0.3$, unless the jet actually consists of a series of discrete segments that have very different Lorentz factors (see Section 4.4 for a specific example). On the other hand, the jet could be angularly structured, and the LOS somewhat deviates from the symmetry axis of the jet (E. Rossi et al. 2002; B. Zhang & P. Mészáros 2002). This is possible if the nondetection of high-energy emission in EP241021a

(Section 2.2) is due to an off-axis viewing angle. Then, as the emission from the core of the jet gradually enters the view, a rising afterglow can be obtained. Here, in order to explain the fast jump of the emission, the jet should consist of two or more separated angular components, which could specifically correspond to the core, wing, and cocoons of the jet (see G. Gianfagna et al. 2025 for detailed modeling). In this case, since the LOS initially pointed to the wide slow component, optical and X-ray bumps can be produced when the narrow fast component suddenly emerges in the view at a later time (J. Granot et al. 2002; R. Yamazaki et al. 2004; F. Xu et al. 2023b; B. O'Connor et al. 2024). Such a nonthermal origin of both optical and X-ray brightenings is further beneficial for explaining the hard X-ray spectrum and the relatively red color of the optical emission.

To model the multiwavelength light curves in the twocomponent jet scenario, we use mainly the optical r-band data taken from our follow-up observations, GCN Circulars, and the data set presented by M. Busmann et al. (2025), in which the bump features are more clearly presented. All the fluxes have been corrected for the Galactic extinction. For the radio data, we mainly utilize the flux densities observed at 5 GHz and 9 GHz, as they are less affected by the ISS and are relatively well sampled. In addition to data provided in Table 2, we retrieve the relevant data observed by ATCA (program ID CX585), consisting of eight observations. We then produce the calibrated clean images and measure the flux densities at 5 GHz and 9 GHz, following the procedures described in Section 2.5.4. However, the fitting to the multiwavelength light curves with a structured jet yields an unphysically high Lorentz factor (exceeding 1000) for the fast, narrow jet. Furthermore, this model fails to account for the third optical bump observed around 20 days after the burst. The optical flux observed after this bump is also significantly higher than that predicted by the model.

If EP241021a is related to a GRB, the missing prompt gamma rays might imply a low-luminosity burst. In this case, the absence of a supernova disfavors a GRB 980425–like event that is associated with a "hypernova" (K. Iwamoto et al. 1998), and its nonthermal spectrum differs from the thermal SBO source GRB 060218 (S. Campana et al. 2006), pointing to a distinct subclass. In any case, M. Xu & Y. F. Huang (2012) identified a tight relation linking the luminosity and duration of the plateau to the isotropic-equivalent gamma-ray energies. As shown in Figure 7, EP241021a deviates significantly from this relation, suggesting a possibly different origin for the X-ray emission as observed in conventional GRBs.

4.4. Multiple Jet Ejections from Repeating Partial TDEs

4.4.1. Modeling the Multiwavelength Light Curves with Three Jets Launched at Separate Times

The discrepancies of modeling with a two-component structured jet motivate us to explore an alternative explanation. We thus turn to the scenario involving three jet ejections, in which the two late-time optical bumps arise from the interactions of two additional jets launched a few days after the initial one. Following the approach outlined by Y. F. Huang et al. (2000), we calculate the jet dynamics and associated synchrotron emission separately for each of the

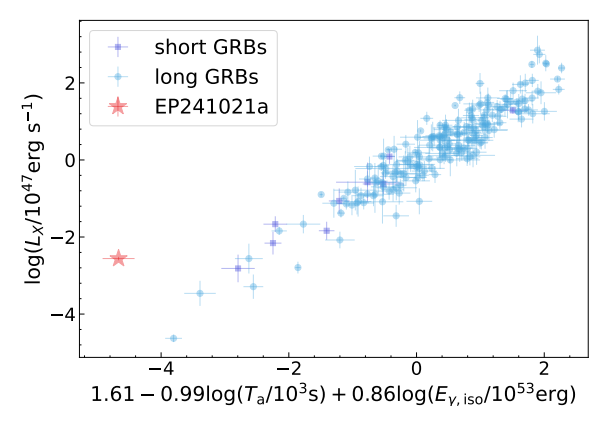


Figure 7. EP241021a and the observed *L-T-E* relation for 210 GRBs (F. Xu et al. 2021; C. Deng et al. 2023). Long GRBs and short GRBs are marked with blue circles and purple squares, respectively. EP241021a is an outlier of this relation, indicating that its plateau originates from a different mechanism compared to the typical GRB plateau.

three jet components (see also F. Xu et al. 2023a). The MCMC algorithm is employed to constrain the model parameters. The subscripts "1," "2," and "3" denote the first, second, and third jets, respectively. Determining the opening angles of all three jets is challenging owing to the absence of a clear jet break in the light curve. As a result, the opening angles of all three jets are fixed at 0.1 rad and assumed to be viewed on-axis.

The best-fit models to match the multiwavelength light curves are plotted in the left panel of Figure 8. In the right panel of Figure 8, we illustrate the evolution of the kinetic energy, radius, and Lorentz factor for the three jets. The bestfit results are presented in Table C1, while the corresponding corner plot is shown in Figure C1. The inferred initial Lorentz factors are $\Gamma_1 \approx 20$ for the first jet, $\Gamma_2 \approx 9$ for the second, and $\Gamma_3 \approx 7$ for the third, indicating that all three outflows are mildly relativistic. The Lorentz factors are not at odds with that constrained by the radio SED fittings and the equipartition analysis (Section 3.3), though only one jet shocking synchrotron emission component was assumed for the latter. The isotropic kinetic energies are estimated to be 1.1×10^{54} erg for the first jet, 7.5×10^{52} erg for the second, and 5.0×10^{52} erg for the third. The time interval between the first and second jets is constrained to \sim 2.9 days in the rest frame, while the interval between the second and third jets spans about 7 days in the rest frame. We note that the model underpredicts the X-ray emission, suggesting that an additional emission component is required, perhaps from the internal dissipation process within the jet powered by an active central engine (I. Andreoni et al. 2022; Y. Yao et al. 2024). We will discuss the interesting implications of the three-jet model in the next section.

4.4.2. Constraints on the Black Hole Mass in the Context of TDEs

The long-lived X-ray emission may be attributed to a stellar tidal disruption, in which an extreme accretion episode onto a black hole produces relativistic jet ejections. Thus, EP241021a could be a rare jetted TDE. So far, only four TDEs with relativistic jets have been disclosed, with the latest being AT 2022cmc (I. Andreoni et al. 2022). Jetted TDEs are generally characterized by luminous X-ray and radio emission, as well as rapid variability in the early X-ray emission on timescales as short as $\sim\!100\,\mathrm{s}$ (V. Mangano et al. 2016;

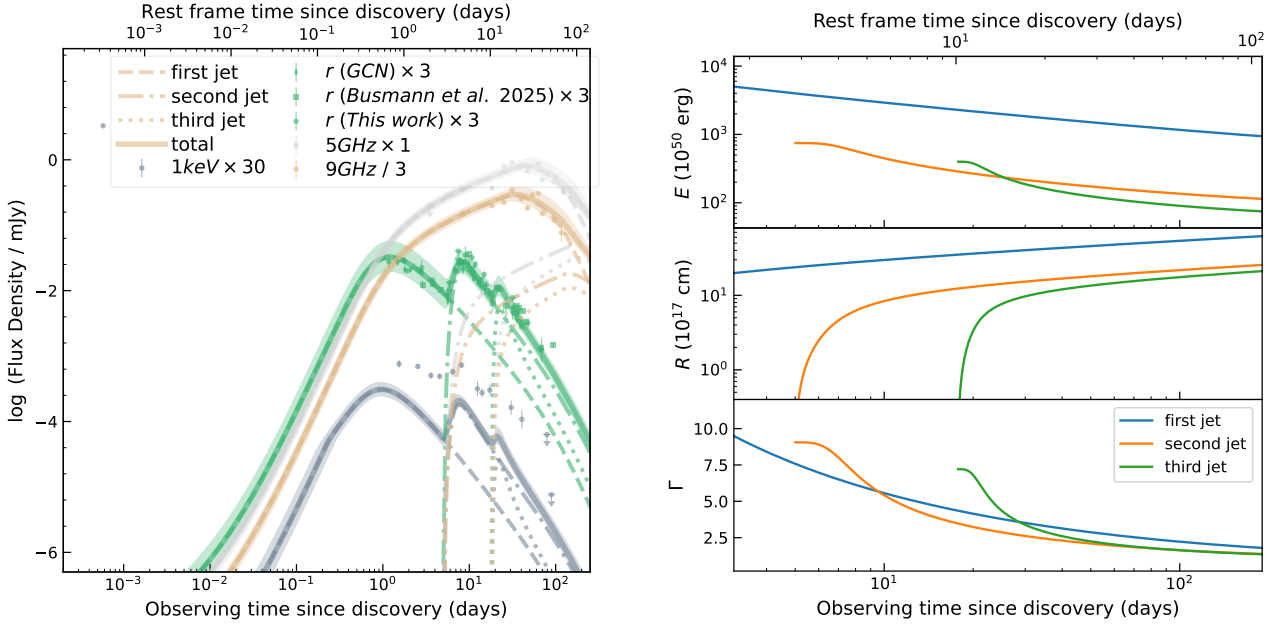


Figure 8. Left: observed multiwavelength afterglow of EP241021a and best-fit results from the three-jet model (solid curves). Shaded regions exhibit the 1σ confidence intervals of the model light curves derived from posterior distributions of model parameters. Both optical and radio light curves are well explained by this model, while the X-ray emission is underpredicted. A possible solution to this inconsistency is the inclusion of a jetted TDE (see Section 4.4). Right: the evolution of the kinetic energy, radius, and Lorentz factor for the three jets. The first, second, and third jets are represented by the blue, orange, and green curves, respectively.

D. R. Pasham et al. 2023). In Swift J1644+57, the prototype of jetted TDEs, the X-ray flux can vary by more than 2 orders of magnitude in the first several days since trigger, with multiple brief flares lasting for $\sim 10^3 - 10^4$ s (J. H. Krolik & T. Piran 2011). The large-amplitude flares could result from geometric effects due to erratic "wobbling" of the jet during the alignment process between the jet and black hole spin axis (A. Tchekhovskov et al. 2014; O. Teboul & B. D. Metzger 2023; W. Lu et al. 2024). In this case, the prompt X-ray emission of EP241021a may be related to a misaligned precessing jet, which can temporarily point along our LOS, causing bright X-ray flares with durations of $\sim 10^2 - 10^3$ s (e.g., A. Tchekhovskoy et al. 2014). It is possible that other flares (if present) may have lower luminosities and hence escaped detection by EP/WXT (W. Yuan et al. 2025). Note that in the context of TDEs, precessing jets are initially choked by an accretion-disk wind, which can only break out of the wind confinement if the misalignment angle is sufficiently small, such as $\theta_{LS} \lesssim 15^{\circ}-20^{\circ}$ (W. Lu et al. 2024). The observed duration for the prompt emission (\sim 100 s) of EP241021a can be used to place an upper limit on the size of the X-rayemitting $R_{\rm X} \lesssim c \Gamma_{\rm i}^2 t_{\rm var}/(1+z) = 1.7 \times 10^{14} (\Gamma_{\rm j}/10)^2$ cm. By requiring

 $M_{\rm BH} \lesssim 5.7 \times 10^6 M_{\odot}$. Our deep XMM-Newton limit at $t_{\rm rest} \approx 50$ days indicates a decrease in the X-ray flux by a factor of $\gtrsim 10$ and a deviation from the earlier power-law decline. Such a sudden decrease could be interpreted as an accretion-state transition from superto sub-Eddington, leading to the cessation of jet ejections, as observed in other jetted TDEs (T. Eftekhari et al. 2024). In the scenario of a TDE, we can estimate the black hole mass ($M_{\rm BH}$) of EP241021a by equating the X-ray luminosity at shutoff to

that $t_{\text{var}}/(1 + z)$ exceeds the light-crossing time of the

Schwarzschild radius of a black hole with mass $M_{\rm BH}$, we find

the Eddington luminosity (T. Eftekhari et al. 2024), such that

$$M_{\rm BH} = 8.4 \times 10^4 \frac{L_{\rm jet}, \, \rm off}{10^{45} \, \rm erg \, s^{-1}} \left(\frac{\epsilon_{\rm disk}}{\epsilon_{\rm jet}} \right) f_{\rm beam}^{-1}, \, 200 f_{\rm bol}, \, 3 \, M_{\odot},$$
(3)

where $L_{\rm jet,off}$ is the breaking luminosity at the time of jet shutoff ($\sim 2.5 \times 10^{43} \, {\rm erg \, s^{-1}}$). The terms $\epsilon_{\rm disk}$ and $\epsilon_{\rm jet}$ represent the radiative efficiencies of the disk and jet, respectively. As before, we adopt a jet half-opening angle $\theta_c = 0.1 \, {\rm rad}$, yielding the jet beaming factor $f_{\rm b} = 200$. Following T. Eftekhari et al. (2024), by assuming $\epsilon_{\rm jet}/\epsilon_{\rm disk} \gtrsim 0.1 \, {\rm and} \, a \, {\rm bolometric}$ correction to the jet luminosity $f_{\rm bol} = 3f_{\rm bol,3}$, we obtain a black hole mass $M_{\rm BH} \lesssim 10^4 \, M_{\odot}$, making EP241021a a possibly jetted TDE involving an IMBH. On the other hand, if the fast rise time ($t_{\rm rest} \approx 1.3 \, {\rm days}$) in the second optical bump is related to the fallback timescale of the disrupted stellar material, which is given by

$$t_{\rm fb} = (3.5 \times 10^5) \left(\frac{M_{\rm BH}}{10^4 \, M_{\odot}}\right)^{1/2} \left(\frac{m_*}{M_{\odot}}\right)^{-1} \left(\frac{r_*}{R_{\odot}}\right)^{3/2} \, {\rm s}, \quad (4)$$

where m_* is the mass of the disrupted star and r_* represents its radius for a main-sequence star, the implied black hole mass is $\sim 10^3 \, M_{\odot}$ for a solar-type star, supporting the scenario of a TDE by an IMBH.

Finally, at the redshift of EP241021a, the host galaxy is not detected in deep imaging with the DESI-Legacy survey down to a limiting r-band magnitude of 24.5. The host may be fainter than 24.9 mag as observed by the Very Large Telescope (M. Busmann et al. 2025), corresponding to an upper limit on the stellar mass of $<3 \times 10^9 M_{\odot}$. We use a galaxy bulge versus black hole mass relation and the upper limit on EP241021a's host-galaxy mass to obtain an upper limit on the

BH mass, $M_{\rm BH} < 10^6\,M_{\odot}$, which is not at odds with the mass estimates inferred from the timescale and luminosity of the jet shutoff.

4.4.3. Energy and Timescale Considerations for Repeating Partial TDEs

To account for the rebrightening of both the X-ray and optical emission, we invoke a scenario that a star is tidally disrupted by the IMBH more than once—repeating partial TDEs. The timescale of X-ray and optical rebrightenings will then correspond to the orbital period of the surviving stellar core after the first disruption. We consider a main-sequence star initially on a slightly bound orbit. Following each disruption, the accretion of stellar debris onto the IMBH powers a relativistic jet, which accommodates the model of multiple jet ejections discussed previously. The kinetic energy of the jets is $E_{\rm k,iso}\Gamma^{-2}\approx 10^{51}\,{\rm erg}$, where $E_{\rm k,iso}$ and Γ denote the isotropic kinetic energy and Lorentz factor, respectively. The accretion of the stellar debris by an IMBH can generate energy of $\sim 10^{52}\,(\Delta M/0.01\,M_\odot)\,c^2\,{\rm erg}$, which suggests that stellar material of mass as low as $\sim 0.01\,M_\odot$ needs to be tidally stripped off each time in order to fuel the jet (with a jet energy efficiency of $\sim 10\%$.)

Based on this picture, we conduct theoretical calculations to match three key constraints placed by observations. (1) The orbital timescale of the stellar core, after the first disruption, should match the timescales of the X-ray and optical rebrightenings. (2) The overall debris fallback rate $\dot{M}_{\rm fb}$ should decay from super-Eddington to sub-Eddington around the time that the jet is observed to shut off. (3) The accretion of the stellar materials is sufficient to power the observed jet energy.

For the calculation of $\dot{M}_{\rm fb}$ for stars in a bound orbit, we modified the parabolic fallback rate that is given by J. Guillochon & E. Ramirez-Ruiz (2013; assuming a $\gamma = 5/3$ polytropic star) by shifting the debris specific energy E to $E + E_0$, where E_0 is the specific orbital energy of the star. Now, $\dot{M}_{\rm fb}$ is given by $\dot{M}_{\rm fb} = dM/dE \times dE/dt$ with shifted E, aligning with the simulations of eccentric TDEs (K. Hayasaki et al. 2013). We also account for the change of orbital energy of the stellar remnant during a partial disruption following the approach of J.-H. Chen et al. (2024).

We find that the observational constraints mentioned above can be reasonably well satisfied using the model of a $10^4 M_{\odot}$ IMBH partially disrupting a solar-like star. The star initially approaches the IMBH along a bound orbit with eccentricity $e \approx 0.897$ and impact factor $\beta \approx 0.82$. After the first encounter, the star goes through a partial TDE, and the surviving core returns for a second encounter with $e \approx 0.9$ and impact factor $\beta \approx 0.826$, followed by a second partial TDE. After the second TDE, the surviving core returns with $e \approx 0.903$ and impact factor $\beta \approx 0.93$, leading to a complete disruption. To reconcile the energy ratio of the three jets, $(\Delta M_1 c^2)/(\Delta M_2 c^2) \approx (E_{k,iso,1}/E_{k,iso,2})(\Gamma_2/\Gamma_1)^2 \approx 2.4 \text{ and } (\Delta M_2 c^2)/2$ $(\Delta M_3 c^2) \approx (E_{\rm k,iso,2}/E_{\rm k,iso,3})(\Gamma_3/\Gamma_2)^2 \approx 1.6$, the accreted stellar masses in these three encounters are $\sim 0.6 \, M_{\odot}$, $\sim 0.25 \, M_{\odot}$, and $0.15 M_{\odot}$, respectively. We note that the stellar mass-radius relation should deviate from that of a main-sequence star after the encounter. In our calculation, the stellar density has a slight decrease after each encounter, consistent with tidal effects such as tidal heating and tidal spin-up causing the star to expand.

We also show the comparison between $\dot{M}_{\rm fb}$ and the observed data in Figure 9. One can see that the overall fallback rate behavior can well explain the observed rebrightening at \sim 5

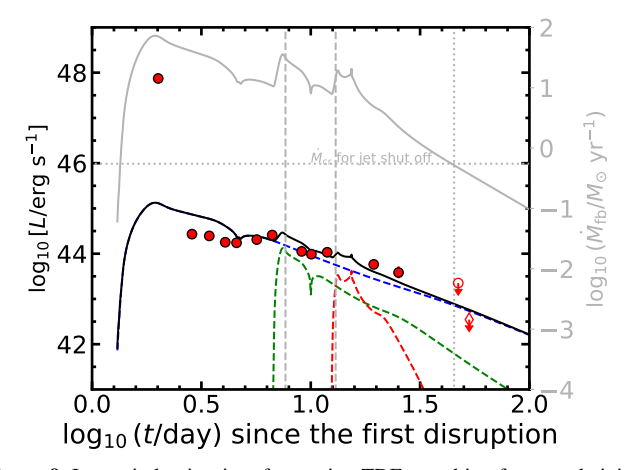


Figure 9. Isotropic luminosity of repeating TDEs resulting from a relativistic jet and the X-ray luminosity in the 0.3–10 keV band. Circular markers denote EP observations, while diamond markers represent XMM-Newton data. Open markers indicate 3σ upper limits. The blue, green, and red dashed lines show the isotropic light curves of the first, second, and third TDEs, respectively. The total light curve (sum of three events; Equation (5)) is illustrated by the solid black line. The solid gray line represents the mass-fallback rate $\dot{M}_{\rm fb}$. The horizontal gray line indicates the critical value of $\dot{M}_{\rm cr}$, marking the transition from a super-Eddington to a sub-Eddington accretion state. The two vertical dashed lines denote the rebrightening time, and the dotted gray line indicates the time at which the jet shuts off.

and 12 days, as well as the accretion-state transition observed at $\sim \! 50$ days after the initial trigger. Subsequent to this transition, $\dot{M}_{\rm fb}$ falls below the critical value $\dot{M}_{\rm cr}$, leading to the jet shutoff. The value of $\dot{M}_{\rm cr}$ is given by $\dot{M}_{\rm cr} \approx L_{\rm Edd}/c^2(R_{\rm disk}/R_{\rm Sch})$ (R.-F. Shen & C. D. Matzner 2014), where $L_{\rm Edd}$, $R_{\rm disk}$, and $R_{\rm Sch}$ are, respectively, the Eddington luminosity, disk radius, and Schwarzchild radius of the IMBH. To match the timing of the X-ray sharp decay, we find that the disk size should be $R_{\rm disk} \approx 20\,R_{\rm p}$, where $R_{\rm p}$ is the pericenter radius of the stellar orbit. This value is reasonable for a typical TDE, where the initial disk experiences modest expansion due to viscous shear.

The inferred isotropic luminosity is given by

$$L \approx \eta \dot{M}_{\rm fb} c^2 \Gamma^2,$$
 (5)

where η is the efficiency of converting accretion power into jet radiative energy and the values of Γ for the three jets are taken to be 18, 9.3, and 6.8, as derived from previous calculations. For matching the overall level of the X-ray flux, a very small η value ($\sim 10^{-6}$) is needed, suggesting that the jet energy is mostly in the form of kinetic energy instead of radiative energy, which is consistent with recent simulations of super-Eddington jets (L. Dai et al. 2018; B. Curd & R. Narayan 2019).

5. Conclusion

We report the discovery of a peculiar X-ray transient, EP241021a, by EP/WXT on 2024 October 21 and the results of follow-up multiwavelength observations including X-ray, optical, and radio. Our sensitive X-ray observations with EP/FXT and XMM-Newton reveal long-duration X-ray emission lasting for at least 1 month, which is unprecedented among known EFXTs. Both optical and radio counterparts are detected within several days after the trigger, with high peak luminosities in excess of $10^{44} \, \mathrm{erg \, s^{-1}}$ and $10^{41} \, \mathrm{erg \, s^{-1}}$,

respectively. These properties, together with the nonthermal X-ray spectrum, red optical color, X-ray and optical rebrightenings, and fast radio spectral evolution suggest that relativistic jets may have been launched, possibly driven by an active central engine. We have considered a variety of scenarios as origins of EP241021a and favor a magnetar engine or jetted TDE, although neither can perfectly explain the multiwavelength properties.

Observations with the Hubble Space Telescope, and possibly with the James Webb Space Telescope, are encouraged; they should have sufficient sensitivity to potentially unveil the faint host galaxy, once the transient emission has fully disappeared. The detection of the host will enable further exploration of whether the transient position (for example, the radio position from our high-resolution VLBA observations) is spatially coincident with the host light centroid. This is crucial for understanding the nature of EP241021a from a rare jetted TDE involving an IMBH or an off-nuclear extremely unusual stellar explosion. With its unique capability of a wide-field survey and rapid X-ray follow-up observations, EP will discover more transients similar to EP241021a with intermediate evolution timescales of months. Timely and deep multiwavelength monitoring is essential for further characterizing and uncovering their intriguing properties as a potentially new phenomenon.

Acknowledgments

This work was based on data obtained with Einstein Probe, a space mission supported by the Strategic Priority Program on Space Science of the Chinese Academy of Sciences, in collaboration with ESA, MPE, and CNES (grant XDA15310000), the Strategic Priority Research Program of the Chinese Academy of Sciences (grant XDB0550200), and the National Key R&D Program of China (grant 2022YFF0711500).

The data presented in this Letter are based in part on observations made with the Karl G. Jansky Very Large Array, the Very Long Baseline Array, the Australia Telescope Compact Array, MeerKAT, and XMM-Newton. The National Radio Astronomy Observatory is a facility of the U.S. National Science Foundation operated under cooperative agreement by Associated Universities, Inc. The Australia Telescope Compact Array is part of the Australia Telescope National Facility (https://ror.org/05qajvd42), which is funded by the Australian Government for operation as a National Facility managed by CSIRO. The MeerKAT telescope is operated by the South African Radio Astronomy Observatory, which is a facility of the National Research Foundation, an agency of the Department of Science and Innovation. We acknowledge the use of the ilifu cloud computing facility (www.ilifu.ac.za) and the Inter-University Institute for Data Intensive Astronomy (IDIA), a partnership of the University of Cape Town, the University of Pretoria, and the University of the Western Cape. This work has made use of the "MPIfR S-band receiver system" designed, constructed, and maintained by funding of the MPI für Radioastronomy and the Max Planck Society. XMM-Newton is an ESA science mission with instruments and contributions directly funded by ESA Member States and NASA.

Some of the data presented herein were obtained at the W. M. Keck Observatory, which is operated as a scientific partnership among the California Institute of Technology, the University of California, and NASA; the observatory was

made possible by the generous financial support of the W. M. Keck Foundation. KAIT and its ongoing operation were made possible by donations from Sun Microsystems, Inc., the Hewlett-Packard Company, AutoScope Corporation, Lick Observatory, the U.S. NSF, the University of California, the Sylvia and Jim Katzman Foundation, and the TABASGO Foundation. Research at Lick Observatory is partially supported by a generous gift from Google, Inc. Mephisto is developed at and operated by the South-Western Institute for Astronomy Research of Yunnan University (SWIFAR-YNU), funded by the "Yunnan University Development Plan for World-Class University" and "Yunnan University Development Plan for World-Class Astronomy Discipline."

X.S. is supported by the National SKA Program of China (2022SKA0130102) and the National Science Foundation of China (NSFC) through grants 12192220 and 12192221. J.H.C. and L.D. acknowledge the support from the Hong Kong Research Grants Council (HKU106220154, 109000722). C.J. acknowledges the National Natural Science Foundation of China through grant 12473016. Y.X. acknowledges the support of NSFC 12025303. P.O.B. acknowledges support from UKRI under grant ST/W000857/1. R.S. acknowledges INAF grant 1.05.23.04.04. A.K. and J.R.M. are supported by the UK Science and Technology Facilities Council (STFC) consolidated grant ST/V000853/1. F.P. acknowledges support from the Spanish Ministerio de Ciencia, Innovación y Universidades (MICINN) under grant PID2022-141915NB-C21. F.X.A. acknowledges support from the National Natural Science Foundation of China (12303016) and the Natural Science Foundation of Jiangsu Province (BK20242115). T.A. acknowledges the support of the Xinjiang Tianchi Talent Program and FAST Special Program (NSFC 12041301). A.V. F.'s research group at UC Berkeley acknowledges financial assistance from the Christopher R. Redlich Fund, Gary and Cynthia Bengier, Clark and Sharon Winslow, Alan Eustace and Kathy Kwan, William Draper, Timothy and Melissa Draper, Briggs and Kathleen Wood, Sanford Robertson (W.Z. is a Bengier-Winslow-Eustace Specialist in Astronomy, T.G. B. is a Draper-Wood-Robertson Specialist in Astronomy, Y. Y. was a Bengier-Winslow-Robertson Fellow in Astronomy), and numerous other donors. B.K. acknowledges the support from the "Special Project for High-End Foreign Experts," Xingdian Funding from Yunnan Province, the Key Laboratory of Survey Science of Yunnan Province (202449CE340002), and the National Key Research and Development Program of China (grant No. 2024YFA1611603).

Software: Autophot (S. J. Brennan & M. Fraser 2022), Astropy (Astropy Collaboration et al. 2013, 2018, 2022), AIPS (E. W. Greisen 2003), CASA (v6.6.1; J. P. McMullin et al. 2007), DiFX software correlator (A. T. Deller et al. 2011), DIFMAP (M. C. Shepherd 1997), IRAF (D. Tody 1986), LPipe (D. A. Perley 2019), Miriad (R. J. Sault et al. 1995), OxKAT (I. Heywood 2020), Pypeit (J. Prochaska et al. 2020).

Appendix A Summary of Results from Optical Photometry and Spectroscopy

The log of optical photometry observations and results is given in Table A1. Figure A1 shows the comparison of the optical spectra observed by GTC and Keck (Section 2.4).

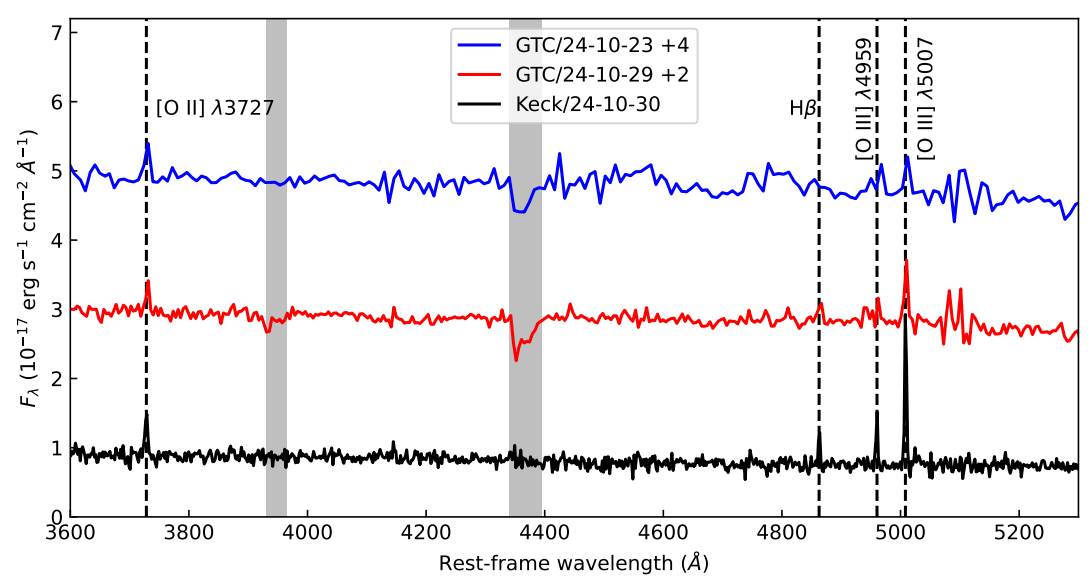


Figure A1. The optical spectrum observed by GTC and Keck on $\Delta t = 2$, 8, and 9 days since the discovery of EP241021a . While the GTC spectra have lower resolution and lower S/N than the Keck spectrum, the narrow emission lines of [O III] λ 5007, [O III] λ 4959, and [O II] λ 3727 are detected, confirming the Keck redshift of z = 0.7478.

Table A1Summary of Optical Observations

Table A1 (Continued)

Summary of Optical Observations				(Continued)			
Time (days)	Band	Magnitude ^a	Telescope	Time (days)	Band	Magnitude ^a	Telescope
1.13	Clear	>18.3	BOOTES-7	8.27	g	21.82 ± 0.25	LCO
1.14	g	>17.5	BOOTES-7	8.28	i	21.12 ± 0.35	LCO
1.14	Clear	21.20 ± 0.20	KAIT (Vega)	8.42	v_m	22.10 ± 0.38	Mephisto
1.15	r	>18.8	BOOTES-7	8.42	r_m	21.32 ± 0.21	Mephisto
1.17	V	21.70 ± 0.30	TRT-SRO	8.42	z_m	>21.29	Mephisto
1.17	R	21.60 ± 0.30	TRT-SRO	8.43	u_m	>22.48	Mephisto
1.76	r	21.55 ± 0.13	LT	8.43	g_m	>22.92	Mephisto
1.77	g	22.04 ± 0.22	LT	8.43	i_m	>22.33	Mephisto
1.77	z	21.60 ± 0.11	NOT	8.86	r	21.77 ± 0.45	LCO
1.91	r	21.95 ± 0.06	NOT	8.9	g	21.98 ± 0.35	LCO
2.07	r	21.88 ± 0.11	LCO	8.96	g	21.96 ± 0.36	LCO
2.08	i	21.73 ± 0.11	LCO	8.93	g	21.69 ± 0.20	LT
2.12	Clear	21.70 ± 0.30	KAIT (Vega)	8.96	z	21.04 ± 0.32	LT
2.7	r	22.29 ± 0.61	LCO	8.96	$\stackrel{\sim}{B}$	>22.10	TRT-SRO
2.71	g	22.38 ± 0.44	LCO	8.89	i	21.42 ± 0.38	LCO
2.76	r	21.96 ± 0.03	NOT	8.98	r	21.77 ± 0.29	LCO
2.79	i	21.86 ± 0.51	LCO	8.99	i	21.38 ± 0.33	LCO
2.80	g	22.06 ± 0.18	LT	8.99	\overline{V}	21.14 ± 0.25	TRT-SRO
2.81	r	21.83 ± 0.30	LT	9.01	R	21.35 ± 0.34	TRT-SRO
2.82	i	21.60 ± 0.18	LT	9.03	I	>20.3	TRT-SRO
2.82	z	21.72 ± 0.11	NOT	9.3	g	22.11 ± 0.27	LCO
2.83	z	21.78 ± 0.20	LT	9.33	r	21.79 ± 0.29	LCO
2.93	R	21.92 ± 0.16	1.5m-OSN	9.33	i	21.45 ± 0.37	LCO
3.72	g	22.52 ± 0.35	LT	9.42	v_m	22.12 ± 0.30	Mephisto
3.73	i	21.92 ± 0.19	LT	9.42	r_m	22.03 ± 0.28	Mephisto
3.77	r	22.30 ± 0.04	NOT	9.42	z_m	>21.47	Mephisto
3.79	z	22.07 ± 0.12	NOT	9.62	g	22.27 ± 0.41	LCO
5.90	r	>22.4	NOT	9.63	r	22.15 ± 0.44	LCO
6.55	r	>20.3	ALT-50A	9.63	i	22.14 ± 0.77	LCO
7.46	R	>21.2	TRT-SBO	9.64	g	22.03 ± 0.11	LCO
7.76	g	21.73 ± 0.07	LT	9.65	r	21.67 ± 0.13	LCO
7.78	i	21.27 ± 0.06	LT	9.71	g	21.89 ± 0.21	LT
7.90	r	21.58 ± 0.12	LT	9.72	i	21.25 ± 0.08	LT
7.92	r	21.64 ± 0.03	NOT	9.73	r	21.66 ± 0.31	LT
7.92	z	20.93 ± 0.16	LT	9.73	z	20.95 ± 0.22	LT
7.93	z	21.31 ± 0.08	NOT	9.78	r	21.77 ± 0.03	NOT
8.26	r	21.5 ± 0.27	LCO	9.80	z	21.33 ± 0.06	NOT

Table A1 (Continued)

Time Band Magnitude ^a (days) 9.86	Telescope
	LCO
	LCO
9.88 g 21.96 ± 0.31	LCO
9.96 g 22.1 \pm 0.33	LCO
9.96 i 21.98 \pm 0.65	LCO
9.97 r 21.84 \pm 0.38	LCO
10.35 g 22.34 \pm 0.45	LCO
10.38 i 21.65 \pm 0.57	LCO
v_m 22.48 ± 0.35	Mephisto
10.00	Mephisto
10.20	Mephisto
***	LCO
10.39 r 22.17 \pm 0.57	
10.74 g 22.25 \pm 0.22	LT
10.74 i 21.33 \pm 0.11	LT
10.75 r 21.45 \pm 0.16	LT
10.76 z 21.11 \pm 0.17	LT
11.72 g 22.12 \pm 0.16	LT
11.73 i 21.92 \pm 0.14	LT
11.74 r 21.70 \pm 0.13	LT
11.74 z 21.33 \pm 0.49	LT
12.74 r 22.40 \pm 0.07	NOT
13.36 v_m 22.54 \pm 0.40	Mephisto
r_m 22.49 \pm 0.38	Mephisto
$z_m > 21.37$	Mephisto
13.88 $z > 21.8$	NOT
13.97 r 22.53 \pm 0.20	LCO
13.98 i 21.86 \pm 0.15	LCO
14.37 $v_m > 21.90$	Mephisto
14.37 $r_m > 22.42$	Mephisto
14.37 $z_m > 20.65$	Mephisto
14.72 g 22.54 \pm 0.11	LT
i 21.86 ± 0.10	LT
1107	LT
14.85 g 22.53 ± 0.25 14.86 r 22.09 ± 0.12	LT
i 22.09 \pm 0.12 14.86 i 22.12 \pm 0.18	LT
	LT
15.71 g 22.86 \pm 0.27	LT
15.72	LT
15.72 i 22.19 \pm 0.12	LT
15.73 z 21.89 \pm 0.26	LT
18.70 r 22.98 \pm 0.15	NOT
19.80 z 22.50 \pm 0.20	NOT
27.39 $r > 20.0$	NanShan-HMT
$30.00 r 23.70 \pm 0.20$	SVOM/VT
31.71 $r > 22.98$	LT
31.72 g >23.01	LT
31.74 i 22.35 ± 0.32	LT
31.75 $z > 22.23$	LT
37.47 r >22.9	ALT-100C
37.52 $z > 21.1$	ALT-100C
38.68 r 23.89 ± 0.22	NOT
r > 22.9	ALT-100C
39.43 z >21.4	ALT-100C
77.77 r 23.94 ± 0.18	GTC
48.76 i 23.50 ± 0.23	NOT
	NOT
68.83	NOT NOT
13.01 t 43.01 ± 0.20	NOI

Note

Appendix B Fittings to the X-Ray Light Curve

Figure B1 shows the X-ray light curve of EP241021a (filled red stars and downward arrows) and the best-fit model realizations from MCMC fittings (gray curves). The light curve is modeled using a smoothed broken power-law function. The function takes the following form as presented by T. Eftekhari et al. (2024):

$$F_{\rm X}(t) = F_{\rm X} \left[\left(\frac{t}{t_{\rm off}} \right)^{-s\alpha_1} + \left(\frac{t}{t_{\rm off}} \right)^{-s\alpha_2} \right]^{-\frac{1}{5}}.$$

In order to incorporate the information provided by the upper-limit points into the fitting process, we redefine the likelihood function (T. Eftekhari et al. 2024),

$$\mathcal{L} = \prod_i p(e_i)^{\delta_i} F(e_i)^{1-\delta_i},$$

where $\delta_i = 0$ denotes a data point without detection and $\delta_i = 1$ represents the detection data point. We have

$$F(e_i) = \frac{1}{2} \left[1 + \operatorname{erf}\left(\frac{e_i}{\sqrt{2}\sigma_i}\right) \right],$$

where erf is the error function and σ_i represents the Poisson single-sided upper limits for data points without detection.

We find that the fit cannot adequately capture the last two upper-limit points. To address this issue, we introduce a third power-law segment into the fitting formula and omit the smoothing factor. The resulting functional form is

$$F_{X}(t) = \begin{cases} F_{01} \left(\frac{t}{t_{01}}\right)^{\alpha_{0}}, & t < t_{01} \\ F_{01} \left(\frac{t}{t_{01}}\right)^{\alpha_{1}}, & t_{01} \leqslant t < t_{02} \end{cases}$$

$$F_{01} \left(\frac{t_{12}}{t_{01}}\right)^{\alpha_{1}} \left(\frac{t}{t_{12}}\right)^{\alpha_{2}}, & t \geqslant t_{12}.$$

Here, α_0 , α_1 , and α_2 denote the power-law indices of the three segments, t_{01} and t_{12} represent the respective times of the first and second breaks, and F_{01} denotes the flux at the first break time

In Figure B2, we also show the best-fit model realizations to the X-ray light curve using the three piecewise power-law model. In comparison with the broken power-law function, we found that the Bayes factor K=4.12, where $K=\exp(\log Z_1 - \log Z_2)$, and Z_1 and Z_2 are known as the marginal likelihood or Bayesian evidence (J. Buchner 2023). This suggests that the fitting with the piecewise power law is statistically better than the broken power-law function. Therefore, our analysis of the X-ray light curve was based mainly on the fitting results with the piecewise power law.

^a The magnitude has not been corrected for Galactic extinction.

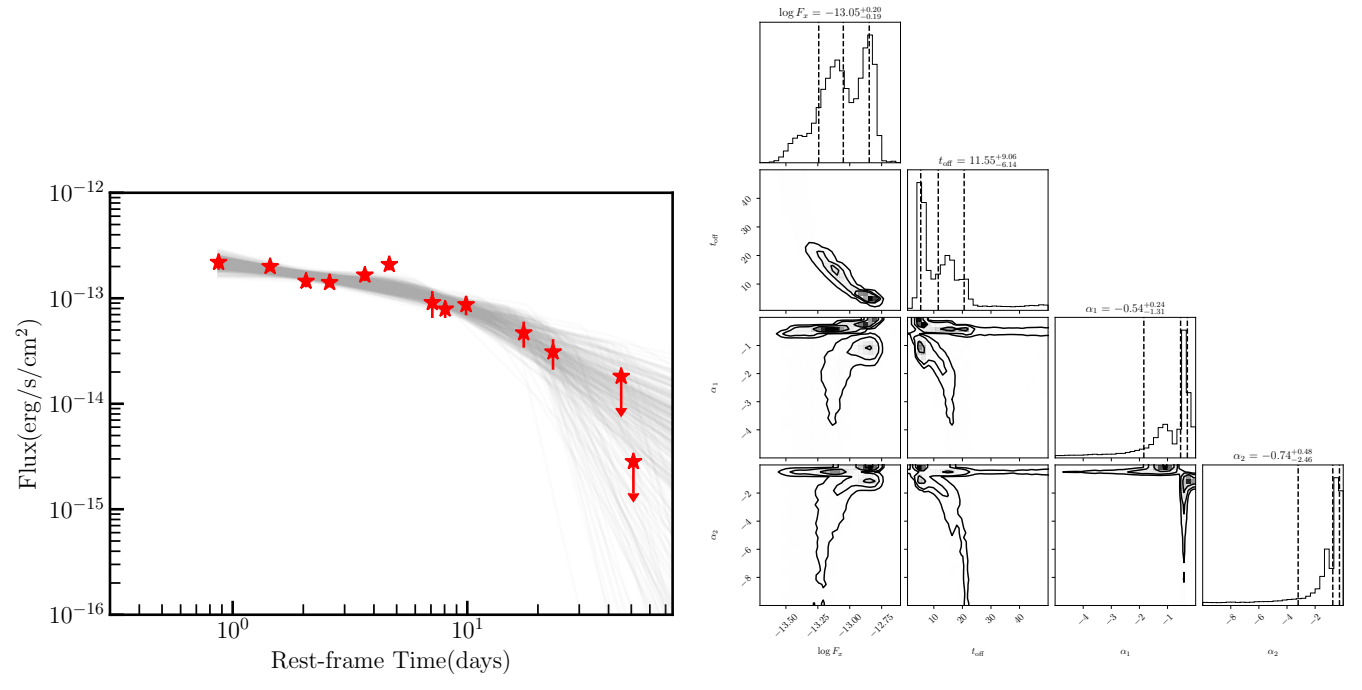


Figure B1. Left: X-ray light curve in the 0.5–4 keV range within \sim 1–50 rest-frame days since discovery. The data are taken from EP/WXT, EP/FXT, and XMM-Newton observations. Our best-fit model with three power laws is shown as gray curves, representing random samples from the MCMC chains. Right: marginalized posterior distributions for each model parameter are shown on the diagonal, where dashed lines indicate the median and 68% confidence interval.

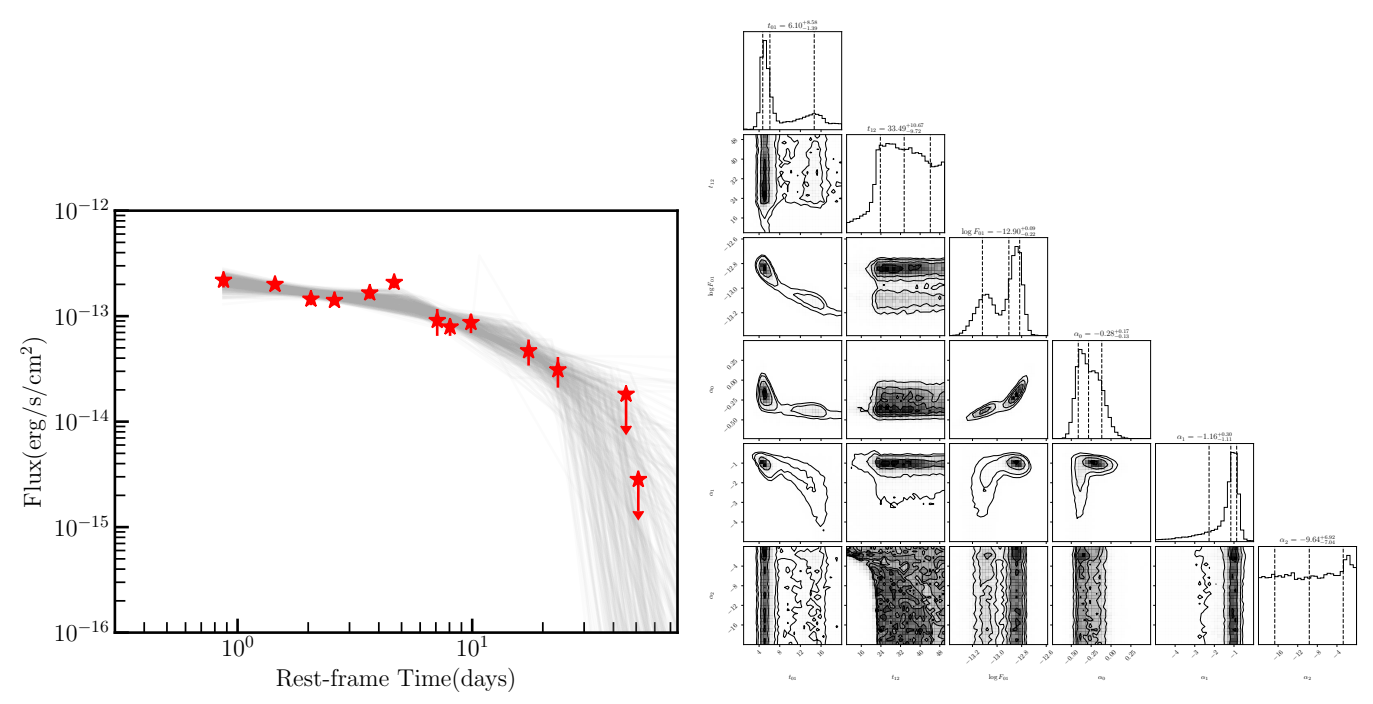


Figure B2. The same as Figure B1 but for the model with three piecewise power laws.

Appendix C Parameter Constraints for the Three-jet Model from the Light-curve Fitting

In this section, we show the corner plot of the multi-wavelength fitting results using the model consisting of three jet ejections (Figure C1) and the constraints on the jet parameters (Table C1).

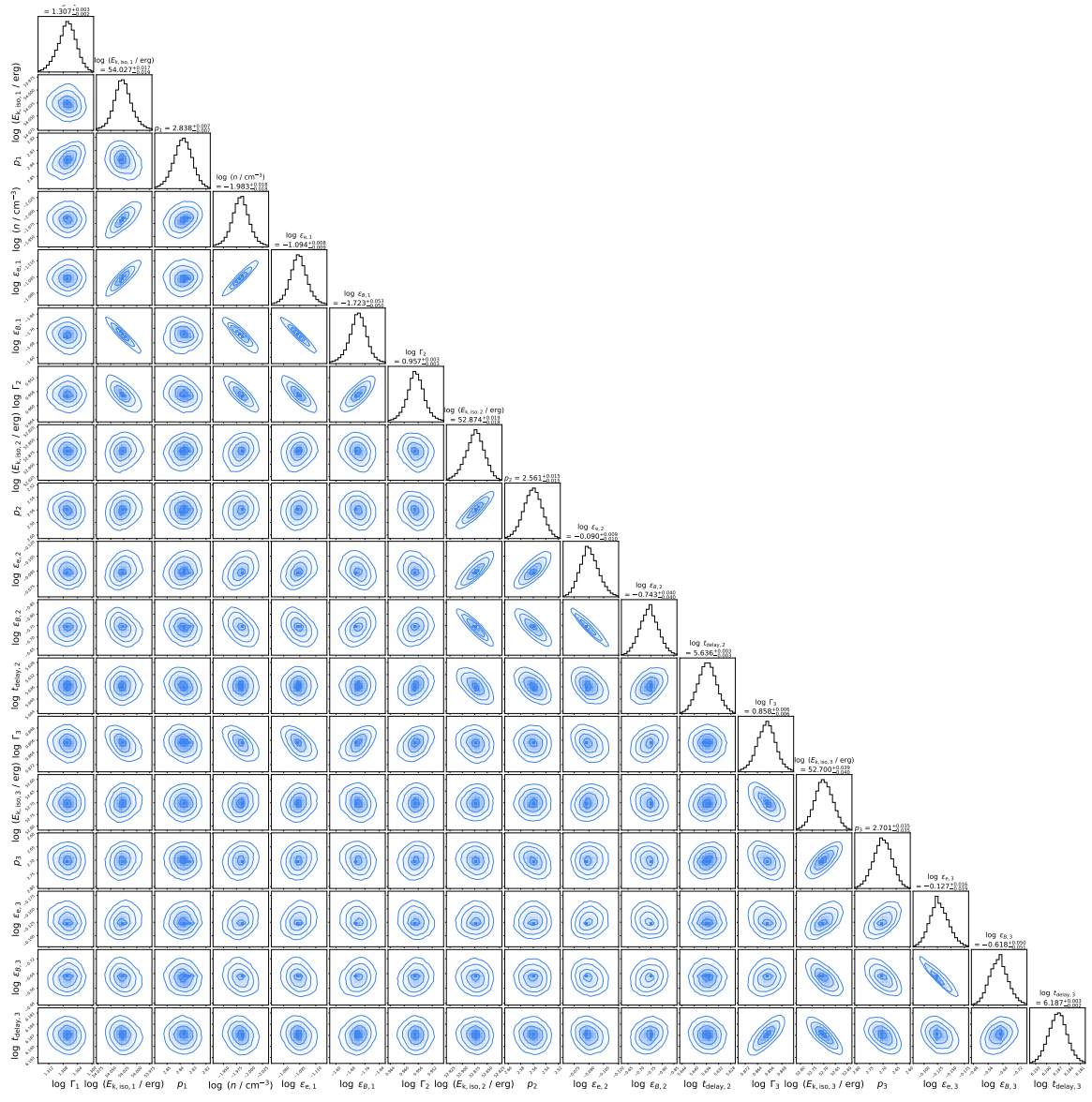


Figure C1. Parameters derived for EP241021a by using the three-jet model. The contour curves represent the $1\sigma-2\sigma-3\sigma$ confidence levels. The best-fit parameter values, along with their 1σ uncertainties, are indicated above the panels of their respective posterior distributions.

 Table C1

 Parameter Constraints for the Three-jet Model from the Light-curve Fitting

Parameters ^a	First Jet	Second Jet	Third Jet	
$\log \Gamma$	1.307 ± 0.002	0.957 ± 0.003	0.858 ± 0.006	
$log (E_{k,iso}/erg)$	54.027 ± 0.018	52.874 ± 0.018	52.7 ± 0.04	
p	2.838 ± 0.007	2.561 ± 0.015	2.701 ± 0.035	
$\log \epsilon_e$	-1.094 ± 0.008	-0.09 ± 0.01	-0.127 ± 0.018	
$\log \epsilon_B$	-1.723 ± 0.052	-0.743 ± 0.04	-0.618 ± 0.05	
$\log (n/\text{cm}^{-3})$	-1.983 ± 0.018	•••	•••	
$\log (t_{\text{delay}}/\text{s})$		5.636 ± 0.003	6.187 ± 0.002	

Note.

ORCID iDs

```
Xinwen Shu https://orcid.org/0000-0002-7020-4290
Haonan Yang https://orcid.org/0000-0002-7680-2056
Fan Xu https://orcid.org/0000-0001-7943-4685
Jin-Hong Chen https://orcid.org/0000-0002-3525-791X
Rob A. J. Eyles-Ferris https://orcid.org/0000-0002-
8775-2365
Lixin Dai  https://orcid.org/0000-0002-9589-5235
Rong-Feng Shen https://orcid.org/0000-0001-5012-2362
Luming Sun https://orcid.org/0000-0002-7223-5840
WeiKang Zheng https://orcid.org/0000-0002-2636-6508
Ning Jiang https://orcid.org/0000-0002-7152-3621
Ning-Chen Sun https://orcid.org/0000-0002-4731-9698
Dong Xu https://orcid.org/0000-0003-3257-9435
Arne Rau https://orcid.org/0000-0001-5990-6243
Tinggui Wang https://orcid.org/0000-0002-1517-6792
Xue-feng Wu https://orcid.org/0000-0002-6299-1263
Bing Zhang https://orcid.org/0000-0002-9725-2524
Kirpal Nandra https://orcid.org/0000-0002-7150-9192
Alexei V. Filippenko https://orcid.org/0000-0003-
3460-0103
Frédérick Poidevin https://orcid.org/0000-0002-5391-5568
Roberto Soria https://orcid.org/0000-0002-4622-796X
David S. Aguado https://orcid.org/0000-0001-5200-3973
Fangxia An https://orcid.org/0000-0001-7943-0166
Tao An https://orcid.org/0000-0003-4341-0029
Moira Andrews https://orcid.org/0000-0002-1895-6639
Thomas G. Brink https://orcid.org/0000-0001-5955-2502
Alberto J. Castro-Tirado https://orcid.org/0000-0003-
2999-3563
Joseph Farah https://orcid.org/0000-0003-4914-5625
Shaoyu Fu https://orcid.org/0009-0002-7730-3985
Johan P.U. Fynbo https://orcid.org/0000-0002-8149-8298
Xing Gao https://orcid.org/0000-0002-7292-3109
Xuhui Han https://orcid.org/0000-0002-6107-0147
D. Andrew Howell https://orcid.org/0000-0003-4253-656X
Jingwei Hu https://orcid.org/0000-0002-0779-1947
Brajesh Kumar  https://orcid.org/0000-0001-7225-2475
Weihua Lei https://orcid.org/0000-0003-3440-1526
Dongyue Li https://orcid.org/0000-0002-4562-7179
Xiaowei Liu https://orcid.org/0000-0003-1295-2909
Justyn R. Maund https://orcid.org/0000-0003-0733-7215
```

```
Curtis McCully https://orcid.org/0000-0001-5807-7893
Zexi Niu https://orcid.org/0000-0002-3651-0681
Megan Newsome https://orcid.org/0000-0001-9570-0584
Paul O'Brien https://orcid.org/0000-0002-5128-1899
Yu Pan https://orcid.org/0009-0002-7625-2653
Ismael Pérez-Fournon https://orcid.org/0000-0002-
2807-6459
Walter Silima https://orcid.org/0000-0001-8431-1145
Giacomo Terreran https://orcid.org/0000-0003-0794-5982
Samaporn Tinyanont https://orcid.org/0000-0002-
1481-4676
Junxian Wang https://orcid.org/0000-0002-4419-6434
Yun Wang https://orcid.org/0000-0002-8385-7848
Klaas Wiersema https://orcid.org/0000-0002-9133-7957
Yunfei Xu https://orcid.org/0000-0002-7397-811X
Yongguan Xue https://orcid.org/0000-0002-1935-8104
Yi Yang https://orcid.org/0000-0002-6535-8500
Fabao Zhang https://orcid.org/0009-0003-2754-6898
Juan Zhang https://orcid.org/0000-0001-8869-0672
Zipei Zhu https://orcid.org/0000-0002-9022-1928
```

References

```
Alexander, K. D., Berger, E., Guillochon, J., Zauderer, B. A., &
   Williams, P. K. G. 2016, ApJL, 819, L25
Alp, D., & Larsson, J. 2020, ApJ, 896, 39
Andreoni, I., Coughlin, M. W., Perley, D. A., et al. 2022, Natur, 612, 430
Astropy Collaboration, Price-Whelan, A. M., Lim, P. L., et al. 2022, ApJ,
Astropy Collaboration, Price-Whelan, A. M., Sipőcz, B. M., et al. 2018, AJ,
   156, 123
Astropy Collaboration, Robitaille, T. P., Tollerud, E. J., et al. 2013, A&A,
  558. A33
Barbarino, C., Sollerman, J., Taddia, F., et al. 2021, A&A, 651, A81
Barniol Duran, R., Nakar, E., & Piran, T. 2013, ApJ, 772, 78
Barniol Duran, R., & Piran, T. 2013, ApJ, 770, 146
Bauer, F. E., Treister, E., Schawinski, K., et al. 2017, MNRAS, 467, 4841
Berger, E., Zauderer, A., Pooley, G. G., et al. 2012, ApJ, 748, 36
Brennan, S. J., & Fraser, M. 2022, A&A, 667, A62
Buchner, J. 2021, JOSS, 6, 3001
Buchner, J. 2023, StSur, 17, 169
Buchner, J., Georgakakis, A., Nandra, K., et al. 2014, A&A, 564, A125
Burns, E., Ravasio, M. E., Jonker, P. G., Goldstein, A. & Fermi-GBM Team
   2024, GCN, 37855, 1, https://gcn.nasa.gov/circulars/37855
Busmann, M., O'Connor, B., Sommer, J., et al. 2025, arXiv:2503.14588
Campana, S., Mangano, V., Blustin, A. J., et al. 2006, Natur, 442, 1008
Carotenuto, F., Bright, J., & Fender, R. 2024, GCN, 38014, 1, https://gcn.
  nasa.gov/circulars/38014
Cendes, Y., Alexander, K. D., Berger, E., et al. 2021, ApJ, 919, 127
Cenko, S. B., Krimm, H. A., Horesh, A., et al. 2012, ApJ, 753, 77
Chambers, K. C., Magnier, E. A., Metcalfe, N., et al. 2016, arXiv:1612.05560
Chen, C., Wang, Y., & Zhang, B. 2025, arXiv:2505.01606
Chen, J.-H., Dai, L., Liu, S.-F., & Ou, J.-W. 2024, ApJ, 977, 80
Chen, X., Kumar, B., Er, X., et al. 2024, ApJL, 971, L2
Cheng, H., Zhang, C., & Ling, Z. 2025, arXiv:2505.18939
Cordes, J. M., & Lazio, T. J. W. 2002, arXiv:astro-ph/0207156
Curd, B., & Narayan, R. 2019, MNRAS, 483, 565
Dai, L., McKinney, J. C., Roth, N., Ramirez-Ruiz, E., & Miller, M. C. 2018,
     JL, 859, L20
Deller, A. T., Brisken, W. F., Phillips, C. J., et al. 2011, PASP, 123, 275
Deng, C., Huang, Y.-F., & Xu, F. 2023, ApJ, 943, 126
Eappachen, D., Jonker, P. G., Levan, A. J., et al. 2023, ApJ, 948, 91
Eftekhari, T., Tchekhovskoy, A., Alexander, K. D., et al. 2024, ApJ, 974, 149
Eyles-Ferris, R. A. J., Jonker, P. G., Levan, A. J., et al. 2025, ApJL, 988, L14
Feuillet, L. M., Meléndez, M., Kraemer, S., et al. 2024, ApJ, 962, 104
Filippenko, A. V. 1982, P
                         ASP, 94, 715
```

Filippenko, A. V., Li, W. D., Treffers, R. R., & Modjaz, M. 2001, in ASP

Conf. Ser. 246, IAU Colloq. 183: Small Telescope Astronomy on Global

Scales, ed. B. Paczynski, W. P. Chen, & C. Lemme (San Francisco, CA:

ASP), 121

^a The parameters involved in the three-jet model: Γ and $E_{\rm k,iso}$ denote the initial Lorentz factor and the isotropic kinetic energy, respectively; p represents the power-law index of the electron energy distribution; ϵ_e and ϵ_B are the fractions of energy carried by electrons and magnetic fields, respectively; n is the number density of the circumburst medium; and $t_{\rm delay}$ indicates the time delay between the emergence of the first jet and the subsequent two jets.

```
Foreman-Mackey, D., Hogg, D. W., Lang, D., & Goodman, J. 2013, PASP,
Fu, S. Y., Tinyanont, S., Anutarawiramkul, R., et al. 2024a, GCN, 37842, 1,
  https://gcn.nasa.gov/circulars/37842
Fu, S. Y., Zhu, Z. P., An, J., et al. 2024b, GCN, 37840, 1, https://gcn.nasa.
   gov/circulars/37840
Gianfagna, G., Bruni, G., Piro, L., & Thakur, A. L. 2024, GCN, 37906, 1,
   https://gcn.nasa.gov/circulars/37906
Gianfagna, G., Piro, L., Bruni, G., et al. 2025, arXiv:2505.05444
Gillanders, J. H., Rhodes, L., Srivastav, S., et al. 2024, ApJL, 969, L14
Glennie, A., Jonker, P. G., Fender, R. P., Nagayama, T., & Pretorius, M. L.
  2015, MNRAS, 450, 3765
Granot, J., Panaitescu, A., Kumar, P., & Woosley, S. E. 2002, ApJL, 570, L61
Granot, J., & Sari, R. 2002, ApJ, 568, 820
Granot, J., & van der Horst, A. J. 2014, PASA, 31, e008
Greisen, E. W. 2003, in Information Handling in Astronomy-Historical
   Vistas, ed. A. Heck, 285 (New York: Springer), 109
Guillochon, J., & Ramirez-Ruiz, E. 2013, ApJ, 767, 25
Hamidani, H., Sato, Y., Kashiyama, K., et al. 2025, ApJL, 986, L4
Hayasaki, K., Stone, N., & Loeb, A. 2013, MNRAS, 434, 909
Heywood, I., 2020 oxkat: Semi-automated Imaging of MeerKAT
   Observations, Astrophysics Source Code Library, ascl:2009.003
Ho, A. Y. Q., Perley, D. A., Gal-Yam, A., et al. 2023, ApJ, 949, 120
Hu, J. W., Wang, Y., He, H., et al. 2024, GCN, 37834, 1, https://gcn.nasa.
   gov/circulars/37834
Huang, Y. F., Gou, L. J., Dai, Z. G., & Lu, T. 2000, ApJ, 543, 90
Iwamoto, K., Mazzali, P. A., Nomoto, K., et al. 1998, Natur, 395, 672
Izzo, L., Martin-Carrillo, A., Malesani, D. B., et al. 2025, GCN, 39851, 1,
   https://gcn.nasa.gov/circulars/39851
Jiang, S.-Q., Xu, D., van Hoof, A. P. C., et al. 2025, ApJL, 988, L34
Jonker, P. G., Glennie, A., Heida, M., et al. 2013, ApJ, 779, 14
Kasen, D., Badnell, N. R., & Barnes, J. 2013, ApJ, 774, 25
Kennicutt, R. C., Jr. 1998, ARA&A, 36, 189
Kewley, L. J., Groves, B., Kauffmann, G., & Heckman, T. 2006, MNRAS,
   372, 961
Khatami, D. K., & Kasen, D. N. 2024, ApJ, 972, 140
Kraft, R. P., Burrows, D. N., & Nousek, J. A. 1991, ApJ, 374, 344
Krolik, J. H., & Piran, T. 2011, ApJ, 743, 134
Kumar, A., Maund, J. R., Sun, N. C., et al. 2024, GCN, 37875, 1, https://gcn.
   nasa.gov/circulars/37875
Lacy, M., Baum, S. A., Chandler, C. J., et al. 2020, PASP, 132, 035001
Levan, A. J., Jonker, P. G., Saccardi, A., et al. 2024, arXiv:2404.16350
Li, W. X., Sun, N. C., Maund, J., Wang, Y. N., & Wiersema, K. 2024, GCN,
   37846, 1, https://gcn.nasa.gov/circulars/37846
Li, W. X., Zhu, Z. P., Zou, X. Z., et al. 2025, arXiv:2504.17034
Lin, D., Irwin, J. A., Berger, E., & Nguyen, R. 2022, ApJ, 927, 211
Liu, Y., Sun, H., Xu, D., et al. 2025, NatAs, 9, 564
Liu, Y.-Q., Modjaz, M., & Bianco, F. B. 2017, ApJ, 845, 85
Lovell, J. E. J., Jauncey, D. L., Bignall, H. E., et al. 2003, AJ, 126, 1699
Lu, W., Matsumoto, T., & Matzner, C. D. 2024, MNRAS, 533, 979
Mangano, V., Burrows, D. N., Sbarufatti, B., & Cannizzo, J. K. 2016, ApJ,
  817, 103
Margalit, B., Quataert, E., & Ho, A. Y. Q. 2022, ApJ, 928, 122
McMullin, J. P., Waters, B., Schiebel, D., Young, W., & Golap, K. 2007, in
   ASP Conf. Ser. 376, Astronomical Data Analysis Software and Systems
   XVI, ed. R. A. Shaw, F. Hill, & D. J. Bell (San Francisco, CA: ASP), 127
Metzger, B. D., & Piro, A. L. 2014, MNRAS, 439, 3916
O'Connor, B., Beniamini, P., & Gill, R. 2024, MNRAS, 533, 1629
O'Connor, B., Pasham, D., Andreoni, I., et al. 2025, ApJL, 979, L30
Offringa, A. R., & Smirnov, O. 2017, MNRAS, 471, 301
Oke, J. B., Cohen, J. G., Carr, M., et al. 1995, PASP, 107, 375
Pan, Y., Kumar, B., Lin, W., et al. 2024, GCN, 37968, 1, https://gcn.nasa.
   gov/circulars/37968
Pasham, D. R., Lucchini, M., Laskar, T., et al. 2023, NatAs, 7, 88
```

```
Pérez-Fournon, I., Sun, N. C., Li, W., et al. 2024, GCN, 37858, 1, https://gcn.
  nasa.gov/circulars/37858
Perley, D. A. 2019, PASP, 131, 084503
Prochaska, J., Hennawi, J., Westfall, K., et al. 2020, JOSS, 5, 2308
Quirola-Vásquez, J., Bauer, F. E., Jonker, P. G., et al. 2022, A&A, 663, A168
Quirola-Vásquez, J., Bauer, F. E., Jonker, P. G., et al. 2023, A&A, 675, A44
Quirola-Vásquez, J., Bauer, F. E., Jonker, P. G., et al. 2024, A&A, 683, A243
Rastinejad, J. C., Levan, A. J., Jonker, P. G., et al. 2025, ApJL, 988, L13
Rees, M. J., & Mészáros, P. 1998, ApJL, 496, L1
Ricci, R., Bruni, G., Carotenuto, F., Gianfagna, G., & Yao, Y. 2024, GCN,
  37949, 1, https://gcn.nasa.gov/circulars/37949
Ricci, R., Troja, E., Yang, Y.-H., et al. 2025, ApJL, 979, L28
Rickett, B. J. 2007, A&AT, 26, 429
Rossi, E., Lazzati, D., & Rees, M. J. 2002, MNRAS, 332, 945
Ruiz, A., Georgakakis, A., Gerakakis, S., et al. 2022, MNRAS, 511, 4265
Salafia, O. S., & Ghirlanda, G. 2022, Galax, 10, 93
Sault, R. J., Teuben, P. J., & Wright, M. C. H. 1995, in ASP Conf. Ser. 77,
   Astronomical Data Analysis Software and Systems IV, ed. R. A. Shaw,
  H. E. Payne, & J. J. E. Hayes (San Francisco, CA: ASP), 433
Shen, R.-F. 2019, ApJL, 871, L17
Shen, R.-F., & Matzner, C. D. 2014, ApJ, 784, 87
Shepherd, M. C. 1997, in ASP Conf. Ser. 125, Astronomical Data Analysis
  Software and Systems VI, ed. G. Hunt & H. Payne (San Francisco, CA:
  ASP), 77
Soderberg, A. M., Berger, E., Page, K. L., et al. 2008, Natur, 453, 469
Srinivasaragavan, G. P., Hamidani, H., Schroeder, G., et al. 2025, ApJL,
  988, L60
Srivastav, S., Chen, T. W., Gillanders, J. H., et al. 2025, ApJL, 978, L21
Sun, H., Li, W. X., Liu, L. D., et al. 2025, NatAs, 9, 1073
Sun, H., Zhang, B., & Gao, H. 2017, ApJ, 835, 7
Svinkin, D., Frederiks, D., & Lysenko, A. 2024, GCN, 38304, 1, https://gcn.
   nasa.gov/circulars/38034
Tchekhovskoy, A., Metzger, B. D., Giannios, D., & Kelley, L. Z. 2014,
   MNRAS, 437, 2744
Teboul, O., & Metzger, B. D. 2023, ApJL, 957, L9
Tody, D. 1986, Proc. SPIE, 627, 733
Tsvetkova, A., Frederiks, D., Golenetskii, S., et al. 2017, ApJ, 850, 161
van Dalen, J. N. D., Levan, A. J., Jonker, P. G., et al. 2025, ApJL, 982, L47
Walker, M. A. 1998, MNRAS, 294, 307
Wang, Y., He, H., Yang, S. K., et al. 2024, GCN, 37848, 1, https://gcn.nasa.
  gov/circulars/37848
Wu, G.-L., Yu, Y.-W., Liu, L.-D., et al. 2025, arXiv:2505.12491
Xu, F., Huang, Y.-F., & Geng, J.-J. 2023a, A&A, 679, A103
Xu, F., Huang, Y.-F., Geng, J.-J., et al. 2023b, A&A, 673, A20
Xu, F., Tang, C.-H., Geng, J.-J., et al. 2021, ApJ, 920, 135
Xu, M., & Huang, Y. F. 2012, A&A, 538, A134
Yadav, M., Troja, E., Ricci, R., et al. 2025, arXiv:2505.08781
Yamazaki, R., Ioka, K., & Nakamura, T. 2004, ApJL, 606, L33
Yao, Y., Lu, W., Harrison, F., et al. 2024, ApJ, 965, 39
Yin, Y.-H. I., Zhang, B.-B., Yang, J., et al. 2024, ApJL, 975, L27
Yu, Y.-W., Chen, A., & Li, X.-D. 2019a, ApJL, 877, L21
Yu, Y.-W., Chen, A., & Wang, B. 2019b, ApJL, 870, L23
Yu, Y. W., Liu, X. W., & Dai, Z. G. 2007, ApJ, 671, 637
Yu, Y.-W., Zhang, B., & Gao, H. 2013, ApJL, 776, L40
Yuan, W., Dai, L., Feng, H., et al. 2025, SCPMA, 68, 239501
Zhang, B. 2013, ApJL, 763, L22
Zhang, B., & Mészáros, P. 2002, ApJ, 571, 876
Zhang, W., Yuan, W., Ling, Z., et al. 2025, SCPMA, 68, 219511
Zheng, W., Brink, T. G., Filippenko, A. V., Yang, Y. & KAIT GRB Team
  2024a, GCN, 38294, 1, https://gcn.nasa.gov/circulars/38294
Zheng, W., Han, X., Zhang, P., Filippenko, V. A. & KAIT GRB Team 2024b,
  GCN, 37849, 1, https://gcn.nasa.gov/circulars/37849
Zhu, J.-P., Liu, L.-D., Yu, Y.-W., et al. 2024, ApJL, 970, L42
```

Peng, Z.-K., Yang, Y.-S., Shen, R.-F., et al. 2019, ApJL, 884, L34